# Simulation of secular trends in the middle atmosphere, 1950–2003

R. R. Garcia,[1] D. R. Marsh,[1] D. E. Kinnison,[1] B. A. Boville,[1] and F. Sassi[1]

Received 5 May 2006; revised 7 September 2006; accepted 22 November 2006; published XX Month 2007.

[1] We have used the Whole Atmosphere Community Climate Model to produce a small (three-member) ensemble of simulations of the period 1950–2003. Comparison of model results against available observations shows that for the most part, the model is able to reproduce well the observed trends in zonal mean temperature and ozone, both as regards their magnitude and their distribution in latitude and altitude. Calculated trends in water vapor, on the other hand, are not at all consistent with observations from either the HALOE satellite instrument or the Boulder, Colorado, hygrosonde data set. We show that such lack of agreement is actually to be expected because water vapor has various sources of low-frequency variability (heating due to volcanic eruptions, the quasi-biennial oscillation and El Niño–Southern Oscillation) that can confound the determination of secular trends. The simulations also reveal the presence of other interesting behavior, such as the lack of any significant temperature trend near the mesopause, a decrease in the stratospheric age of air, and the rare occurrence of an extremely disturbed Southern Hemisphere winter.

**Citation:** Garcia, R. R., D. R. Marsh, D. E. Kinnison, B. A. Boville, and F. Sassi (2007), Simulation of secular trends in the middle atmosphere, 1950–2003, *J. Geophys. Res.*, *112*, XXXXXX, doi:10.1029/2006JD007485.



## 1. Introduction

[2] During the second half of the 20th century a variety of anthropogenic compounds were introduced into the atmosphere as a result of industrial activities. In addition to carbon dioxide and other greenhouse gases (GHGs), halogenated compounds were produced in increasing quantities after 1950. The atmospheric effects of these emissions have been the subject of many observational and modeling studies. Recent research on tropospheric warming due to GHGs is documented and summarized in the report of the *Intergovernmental Panel on Climate Change* (IPCC) [2001], while the impact of GHGs and halogenated compounds on the stratosphere, the most dramatic of which is the Antarctic ozone hole, are reviewed in the World Meteorological Organisation (WMO) Assessment of Ozone Depletion [*WMO*, 2003; see also *Austin et al.*, 2003]. As discussed in these reports, current theoretical understanding of atmospheric impacts is based on the results of comprehensive numerical models of the atmosphere. In the case of the stratosphere, the more sophisticated models included in the WMO Assessment take into account coupling between radiatively active gases ($CH_4$, $N_2O$, $O_3$, etc.) and the global circulation that determines in part their distribution in the atmosphere. These models are usually referred to as chemistry-climate models (CCMs). In recent years, considerable effort has been spent in developing increasingly complex CCMs, and in comparing their performance with observations [e.g, *Austin et al.*, 2003; *Manzini et al.*, 2003; *Shine et al.*, 2003; *Austin and Butchart*, 2003; *Dameris et al.*, 2005].

[3] Insofar as CCMs are successful in simulating observed changes and trends in the atmosphere, it is possible to obtain insight into the mechanisms that produce the trends and to gain confidence that the models can be applied to prognostic simulations of the climate on decadal timescales, e.g., to study the recovery of ozone as the atmospheric burden of halogenated gases decreases. In this paper we report the results of a small (three-member) ensemble of simulations of the period 1950–2003 carried out with the Whole Atmosphere Community Climate Model, version 3 (WACCM3). WACCM3 is a CCM that spans the range of altitude from the surface to about 145 km, and incorporates most of the physical and chemical mechanisms believed to be important for determining the dynamical and chemical structure of the middle atmosphere, including the mesosphere and lower thermosphere (MLT).

[4] The simulations described here were carried out as part of the CCM Validation activity of the SPARC program [see *Eyring et al.*, 2006]. SPARC (Stratospheric Processes and their Role in Climate), a "core project" of the World Climate Research Program, is designed to investigate the impact of the stratosphere on global climate, including the upper troposphere/lower stratosphere (UTLS) region, and the troposphere itself. In the present study we analyze the results of the ensemble of WACCM3 simulations and compare them to observations, with emphasis on middle atmosphere trends in temperature, ozone and water vapor over the last two decades of the 20th century. These have been particularly well observed by both ground-based

[1]Earth and Sun Systems Laboratory, National Center for Atmospheric Research, Boulder, Colorado, USA.


0148-0227/07/2006JD007485$09.00

instruments and satellite platforms, and therefore constitute a good test of the ability of the model to simulate climate change in the middle atmosphere. We also touch upon certain other results of the simulations, including the response of the ozone column to solar variability, the lack of long term temperature trends at the mesopause, and changes in stratospheric ‘‘age of air’’ throughout the period of simulation.

[5] Section 2 provides a summary of the numerical model, followed in section 3 by a brief discussion of its climatology. Results on middle atmosphere trends are presented in section 4, and conclusions are summarized in section 5.

## 2. Numerical Model

[6] The Whole Atmosphere Community Climate Model is based on the software framework of the National Center for Atmospheric Research's Community Atmospheric Model (CAM). The current version of the model, WACCM3, which is used in this study, is a superset of CAM, version 3 (CAM3), and includes all of the physical parameterizations of that model. Because of the importance of interactive chemistry in WACCM3, a finite volume dynamical core [*Lin*, 2004], which is an option in CAM3, is used exclusively in WACCM3. This numerical method calculates explicitly the mass fluxes in and out of a given model volume, thus ensuring mass conservation.

[7] The governing equations, physical parameterizations and numerical algorithms used in CAM3 are documented by *Collins et al.* [2004]; only the gravity wave drag and vertical diffusion parameterizations are modified for WACCM3. In addition, WACCM3 incorporates a detailed neutral chemistry model for the middle atmosphere, including heating due to chemical reactions; a model of ion chemistry in the mesosphere/lower thermosphere (MLT); ion drag and auroral processes; and parameterizations of shortwave heating at extreme ultraviolet (EUV) wavelengths and infrared transfer under nonlocal thermodynamic equilibrium (NLTE) conditions. The processes and parameterizations that are unique to WACCM3 are described below; for details on all others, the reader is referred to Collins et al. and to the CAM Web site (http://www.ccsm.ucar.edu/models/atm-cam/).

### 2.1. Domain and Resolution

[8] WACCM3 is a global model with 66 vertical levels from the ground to $4.5 \times 10^{-6}$ mbar (approximately 145 km geometric altitude). As in CAM3, the vertical coordinate is purely isobaric above 100 mbar, but is hybrid below that level. The vertical resolution is variable: 3.5 km above about 65 km, 1.75 km around the stratopause (50 km), 1.1–1.4 km in the lower stratosphere (below 30 km), and 1.1 km in the troposphere (except near the ground where much higher vertical resolution is used in the planetary boundary layer).

[9] WACCM3 currently supports two standard horizontal resolutions: $1.9° \times 2.5°$ and $4° \times 5°$ (latitude × longitude). The simulations presented in this paper, which encompass the 54-year period 1950–2003 and place very large demands on computational resources, have been carried out at $4° \times 5°$ resolution. At all resolutions, the time step is 1800 s for the physical parameterizations. Within the finite volume dynamical core only, this time step is subdivided as necessary for computational stability.

### 2.2. Gravity Wave Parameterization

[10] WACCM3 incorporates a parameterization for a spectrum of vertically propagating internal gravity waves based on the work of *Lindzen* [1981], *Holton* [1982], *Garcia and Solomon* [1985], and *Sassi et al.* [2002]. Orographically generated gravity waves follow the parameterization of *McFarlane* [1987]. Both the orographic and spectral components of the parameterization take into account the rapid increase with altitude of molecular diffusion, which leads to diffusive separation and becomes the principal dissipation mechanism for upward propagating waves. Details of the implementation of these parameterizations in WACCM3 are given in Appendix A.

### 2.3. Molecular Diffusion

[11] Molecular diffusion is included in WACCM3 using the formulation of *Banks and Kockarts* [1973]. Enhanced molecular diffusivity suppresses the breaking of parameterized gravity waves above about 100 km, where wave dissipation occurs mainly via this process. Molecular diffusion also leads to diffusive separation at altitudes where the mean free path becomes large. Since WACCM3 extends only into the lower thermosphere, we avoid the full complexity of the diffusive separation problem by representing the diffusive separation velocity for each constituent with respect to the usual dry air mixture used in the lower atmosphere (mean molecular weight of 28.97 g $mol^{-1}$).

### 2.4. Chemistry

[12] The WACCM3 chemistry module is derived from the three-dimensional (3-D) chemical transport Model for Ozone and Related chemical Tracers (MOZART) [*Brasseur et al.*, 1998; *Hauglustaine et al.*, 1998; *Horowitz et al.*, 2003; http://gctm.acd.ucar.edu/mozart]. It solves for 51 neutral species, including all members of the $O_X$, $NO_X$, $HO_X$, $ClO_X$, and $BrO_X$ chemical families, along with tropospheric ‘‘source species’’ such as the $N_2O$, $H_2O$, $CH_4$, chlorofluorocarbons (CFCs) and other halogenated compounds, etc. Nonmethane hydrocarbons are excluded from this middle atmosphere mechanism, but several ion species important in the MLT ($N_2^+$, $O_2^+$, $N^+$, $NO^+$ and $O^+$, plus electrons) are taken into account. Heterogeneous processes on sulfate aerosols and polar stratospheric clouds (liquid binary sulfate, supercooled ternary solutions, nitric acid trihydrate, and water ice), as well as aerosol sedimentation, are represented following the approach of *Considine et al.* [2000]. In almost all cases the chemical rate constants are taken from JPL02-25 [*Sander et al.*, 2003]. A complete listing of species and reactions is given by *Kinnison et al.* [2006].

[13] The calculation of photolysis rates in WACCM3 is divided into two regions: 120–200 nm (34 wavelength intervals) and 200–750 nm (67 wavelength intervals). The photolysis rate for each absorbing species is calculated during model execution as a function of the exoatmospheric flux, the atmospheric transmission function, the molecular absorption cross section, and the quantum yield. Details are given by *Kinnison et al.* [2006]. The exoatmospheric flux

over the model wavelength intervals is parameterized in terms of the solar 10.7 cm radio flux (f10.7) following *Solomon and Qian* [2005] for wavelengths shortward of Lyman $\alpha$, and *Woods and Rottman* [2002] for wavelengths between Lyman $\alpha$ and 350 nm. Beyond 350 nm, the flux is parameterized by regressing the difference between the total solar irradiance data of *Froelich* [2002] and the integrated flux up to 350 nm onto the 10.7 cm radio flux.

### 2.5. Longwave and Shortwave Heating

[14] WACCM3 retains the longwave (LW) formulation used in CAM3 [*Kiehl and Briegleb*, 1991]. However, modeling of the mesosphere and lower thermosphere requires a suite of LW parameterizations that deal with NLTE of the 15 $\mu$m band of $CO_2$ [*Fomichev et al.*, 1998] and cooling due to NO at 5.3 $\mu$m [*Kockarts*, 1980]. The LW heating/cooling rates produced by these parameterizations are merged smoothly at 65 km with those produced by the standard CAM3 LW code, as recently revised by *Collins et al.* [2002].

[15] Shortwave (SW) heating in the CAM3 formulation employs the $\delta$-Eddington approximation longward of 200 nm [*Briegleb*, 1992]. At altitudes higher than ~70 km, radiation of shorter wavelength must also be included in WACCM3. Heating shortward of 200 nm is obtained from the same wavelength-dependent photolysis module used in the chemistry solver. The bond dissociation energy is subtracted for each $O_2$ and $O_3$ photolytic pathway, leaving only localized thermal heating. The additional energy is stored as chemical potential energy and realized later through 24 exothermic reactions, or lost as airglow through the 762 nm $O_2(^1\Sigma)$ and 1.27 $\mu$m $O_2(^1\Delta)$ emission lines [*Mlynczak and Solomon*, 1993].

[16] Solar energy deposition in the EUV (shortward of Lyman $\alpha$) and X-ray region is handled in a manner similar to longer wavelength ultraviolet radiation, with the spectrum divided into moderate-resolution bands and ionization, dissociation, and heating rates calculated in each band as a function of altitude [*Solomon and Qian*, 2005]. At EUV wavelengths, energy partitioning is complicated by photoionization, which generates energetic photoelectrons that, in turn, cause additional ionization, dissociation and heating, and become particularly important in the lower ionosphere. WACCM3 uses a high-resolution parameterization based upon the 1-D photoelectron model of *Solomon and Qian* [2005] to calculate heating rates due to photoelectrons.

[17] The SW heating rates calculated as described above are merged with those obtained with the CAM3 scheme at approximately 65 km. As in the case of photolysis, all heating rates are scaled by the wavelength-dependent exoatmospheric flux.

### 2.6. Auroral Processes, Ion Drag, and Joule Heating

[18] An auroral parameterization based on existing code from NCAR's Thermosphere-Ionosphere-Mesosphere Electrodynamics General Circulation Model (TIME-GCM) [*Roble and Ridley*, 1987] has been developed for rapid calculation of the total auroral ionization rate, particle precipitation in the polar cusp, and general polar cap precipitation ("polar drizzle"). The parameterization takes as input the hemispheric power (HP) of precipitating auroral electrons, and outputs total ionization rates and neutral heating. HP itself is parameterized as a function of the $K_p$ geomagnetic index [*Maeda et al.*, 1989], which is allowed to vary based upon observations. Once ionization rates are determined, the production rates for the E region ions $N_2^+$, $O_2^+$, $N^+$, $NO^+$ and $O^+$ are calculated. Auroral production of NO can then be determined from the reaction of molecular oxygen and $N(^2D)$, the latter produced through dissociative recombination and charge exchange.

[19] The effects of momentum forcing by ion drag and of Joule heating associated with electric fields, which are particularly important above 110 km at high geomagnetic latitudes, are implemented in WACCM3 following *Dickinson et al.* [1981] and *Roble et al.* [1982], respectively. These models require knowledge of the Earth's electric field, which is parameterized according to the model of *Weimer* [1995] for high latitudes and that of *Richmond et al.* [1980] at low and middle latitudes. The Weimer model uses the interplanetary magnetic field as an input; this is estimated in WACCM3 from $K_p$, which, as in the case of the aurora, is allowed to vary according to observations.

### 2.7. Boundary Conditions

[20] The upper boundary conditions for momentum and for most constituents are the usual zero flux conditions used in CAM. However, in the energy budget of the thermosphere, much of the SW radiation at wavelengths <120 nm is absorbed above 145 km (the upper boundary of the model), where LW radiation is very inefficient. This energy is transported downward by molecular diffusion to below 120 km, where it can be dissipated more efficiently by LW emission. Imposing a zero flux upper boundary condition on heat omits a major term in the heat budget and causes the lower thermosphere to be much too cold. Instead, we use the Mass Spectrometer-Incoherent Scatter (MSIS) model [*Hedin*, 1987, 1991] to specify the temperature at the top boundary as a function of season and phase of the solar cycle. The particular version of the MSIS model used in WACCM3 is NRLMSISE-00 (see http://uap-www.nrl.navy.mil/models_web/msis/msis_home.htm).

[21] For chemical constituents, surface mixing ratios of $CH_4$, $N_2O$, $CO_2$, $H_2$, CFC-11, CFC-12, CFC-113, HCFC-22, H-1211, H-1301, $CCl_4$, $CH_3CCH_3$, $CH_3Cl$, and $CH_3Br$ are specified from observations. The model accounts for surface emissions of $NO_X$ and CO based on the emission inventories described by *Horowitz et al.* [2003]. The $NO_X$ source from lightning is distributed according to the location of convective clouds based on *Price et al.* [1997a, 1997b] with a vertical profile following *Pickering et al.* [1998]. Aircraft emissions of $NO_X$ and CO are included in the model and based on *Friedl* [1997].

[22] At the upper boundary, a zero-flux upper boundary condition is used for most species whose mixing ratio is negligible in the lower thermosphere, while mixing ratios of other species are specified from a variety of sources. The MSIS model is used to specify the mixing ratios of O, $O_2$, H, and N; as in the case of temperature, the MSIS model returns values of these constituents as functions of season and phase of the solar cycle. CO and $CO_2$ are specified at the upper boundary using output from the TIME-GCM [*Roble and Ridley*, 1994]. NO is specified using data from the Student Nitric Oxide Explorer (SNOE) satellite [*Barth et al.*, 2003], which has been parameterized as a function of

latitude, season, and phase of the solar cycle in *Marsh et al.*'s [2004] Nitric Oxide Empirical Model (NOEM). Finally, a global mean value (typical of the sunlit lower thermosphere) is specified for species such as $H_2O$, whose abundance near the top of the model is very small under sunlit conditions, but which can be rapidly transported upward by diffusive separation in polar night (since they are lighter than the background atmosphere). In these cases, a zero flux boundary condition leads to unrealistically large mixing ratios at the model top in polar night.

### 2.8. Specification of Boundary and Initial Conditions for 1950–2003

[23] The boundary conditions in this study are based upon, but not identical to, the specifications for the first reference case (REF1) used in the model intercomparison exercise of *Eyring et al.* [2005, 2006]. These specifications include surface mixing ratios for GHGs defined by scenario A1B of *IPCC* [2001]; surface mixing ratios for halogen compounds taken from Table 4B-2 of *WMO* [2003]; monthly mean sea surface temperatures (SSTs) from the UK Met's Hadley Center data set; chemical and radiative effects of volcanic aerosols; and 11-year solar cycle irradiance variability parameterized in terms of observed f10.7 radio flux.

[24] In our simulations, the surface area density (SAD) of sulfate aerosols is derived from satellite observations by the Stratospheric Aerosol and Gas Experiment (SAGE, SAGE II) and the Stratospheric and Mesospheric Sounder (SAMS), as described by *Thomason et al.* [1997] and updated by D. B. Considine [*WMO*, 2003]. Daily observations of f10.7 (and also of the $K_p$ geomagnetic index) were obtained from the Space Environment Center of the U.S. National Oceanographic and Atmospheric Administration (NOAA) (http://www.sec.noaa.gov). Additional details on the REF1 reference case are given by *Eyring et al.* [2005, 2006].

[25] The WACCM3 calculations differ from the REF1 specification in several respects: SST are prescribed from the global HadISST data set prior to 1981 and from the Smith/Reynolds data set after 1981 [*Hurrell et al.*, 2006]; a QBO is neither generated spontaneously by the model nor specified externally; heating from volcanic aerosols is not included (although the chemical effects thereof are taken into account, as noted above); chemical kinetics follow JPL02-25 [*Sander et al.*, 2003], as noted in section 2.4; and, in addition to solar cycle variations in photolysis and heating, WACCM3 also calculates changes in ion and NO production in the aurora, and changes in ion drag and Joule heating, as explained in section 2.6.

[26] Note that the treatment of the effect of volcanic aerosols in these model calculations is incomplete in that heating due to absorption of solar radiation by the aerosols is neglected. We did not include aerosol heating because we lacked a suitable parameterization thereof at the time the model runs were begun. We were particularly concerned about the effects of heating at the tropical cold point, which, if not accurately modeled, can lead to unrealistically large water vapor mixing ratios in the air entering the stratosphere. Once in the stratosphere, this excess water can persist for years, and can affect ozone chemistry through catalysis by the $HO_X$ family. On balance, we decided it was preferable not to include aerosol heating than to include a heating distribution that might cause the aforementioned problems. Thus any effects of volcanic eruptions on temperature, tropical circulation, and water vapor in the lower tropical stratosphere due to aerosol heating of the lower stratosphere are not included in these runs.

[27] Three realizations of the period 1950–2003 were carried out using the boundary conditions described above. The realizations start from an equilibrated initial state for 1950, which was obtained by integrating the model for at least 10 years with fixed boundary conditions and solar inputs appropriate for 1950. Independent realizations are obtained by introducing small perturbations in the equilibrated initial state.

## 3. Model Climatology

[28] Selected aspects of the climatology of WACCM3 have been compared with observations and with the results of other CCMs by *Eyring et al.* [2006]. Here we limit ourselves to showing that the gross features of the wind, temperature, ozone and water vapor fields are in reasonably good agreement with recent observations. For reasons of space we limit our comparisons to solstice, specifically Southern Hemisphere winter, since the wind and temperature structure in this season has often been difficult to model [see, e.g., *Garcia and Boville*, 1994; *Austin et al.*, 2003].

[29] Figure 1 compares the zonal mean zonal wind calculated with WACCM3 for July (Figure 1a) with the UARS Reference Atmosphere Project (URAP) extended climatology for the same month [see *Swinbank and Ortland*, 2003; *Randel et al.*, 2004a; http://code916.gsfc.nasa.gov/Public/Analysis/UARS/urap/home.html], which is based upon data collected over the period 1992–1998. The WACCM3 results are the average for 1990–1999 of the three realizations in the ensemble described in section 2.8. The Upper Atmosphere Research Satellite (UARS) zonal wind data set is derived from High Resolution Doppler Interferometer (HRDI) measurements in the stratosphere and the MLT, supplemented by analyses from the UK Met (UKMO) data assimilation system for the stratosphere. In the lower mesosphere, which is not covered by either HRDI or the UKMO analyses, balanced winds are calculated from URAP temperature data. The stippling in Figure 1 denotes locations where URAP data are sparse or nonexistent and values are interpolated (0.1–1 mbar) or extrapolated (high latitudes above 0.1 mbar) from other regions. In this and all other figures that include a vertical coordinate, WACCM3 results are displayed in log pressure altitude, $Z = H \ln(p_s/p)$, with $p_0$ = 1000 mbar and $H$ = 7 km.

[30] The WACCM3 simulation captures the main features of the URAP climatology, although there are some notable differences: WACCM3 has somewhat stronger tropospheric jets than observed; it calculates maximum summer easterlies in the upper stratosphere in the subtropics rather than in midlatitudes; and it produces easterly winds above 70 km at high latitudes in the winter hemisphere. The discrepancies in the upper stratosphere and mesosphere may be attributed to the gravity wave parameterization, the results of which depend on a number of adjustable parameters. Although it may be possible to improve the agreement between the model and observations by careful adjustment of these parameters, we have not attempted to do so beyond the general considerations outlined in Appendix A.

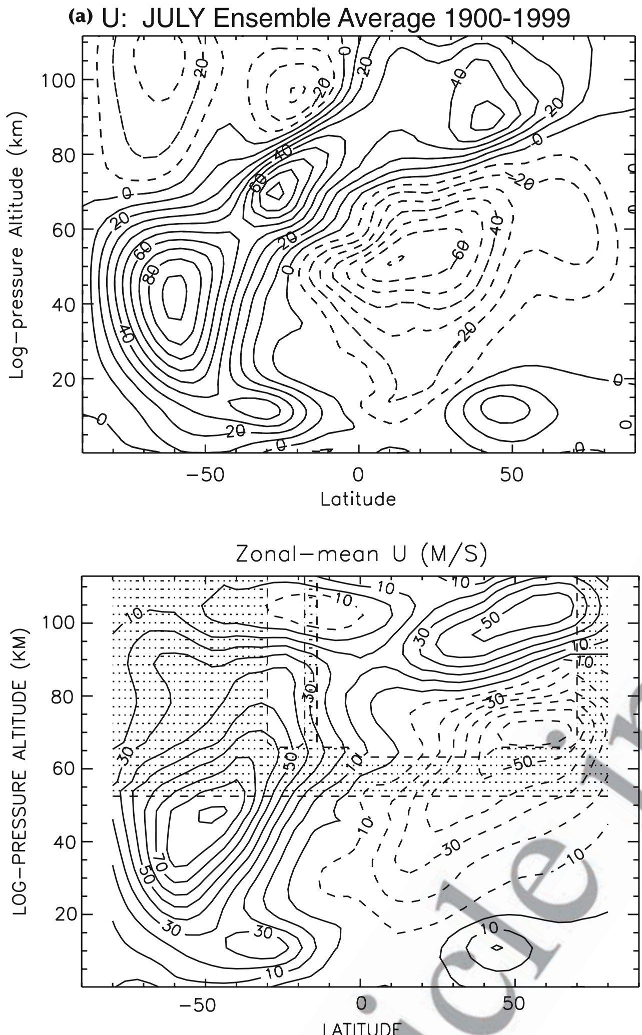


Figure 1. (a) Ensemble mean, zonal mean zonal wind ($m\ s^{-1}$) for July 1990–1999 from the WACCM3 simulations and (b) zonal mean zonal wind from the URAP climatology. The stippling in Figure 1b denotes regions with insufficient coverage, where values are extrapolated or interpolated from other altitudes or latitudes. See text for details.

[31] Perhaps more important than the differences exhibited in Figure 1 is the evolution of the zonal wind (not shown) during the transition from winter to summer in the Southern Hemisphere. In southern winter, the magnitude of WACCM3 winds in the stratosphere is similar to the URAP climatology (e.g., a maximum jet speed of 90 $m\ s^{-1}$), a fact that is also reflected in the lack of a large "cold pole" bias in the middle and upper stratosphere (compare Figure 2). However, these westerly winds remain too strong in October and November and then persist too long into southern summer. At 30 mbar, for example, the transition from westerlies to easterlies at 60 S occurs in January, over a month late compared to UKMO stratospheric wind analyses [see *Eyring et al.*, 2006]. The problem is most apparent in the last two decades of the WACCM3 simulation, when the radiative balance of the Southern Hemisphere lower stratosphere is affected by the formation of the ozone hole. The cold temperatures that develop in the high-latitude lower stratosphere as a result of ozone loss during September and October strengthen the westerlies between 50 and 10 mbar and delay the transition to easterlies, as noted above.

[32] This deficiency of the WACCM3 simulations implies that results for the lower stratosphere of the Southern Hemisphere in late southern spring and early summer must be interpreted with caution. For example, the persistence of cold conditions does not affect the severity of the ozone hole (since ozone depletion has already reached its maximum by mid-October); on the other hand, the persistence of the ozone hole and of westerly winds in the lower stratosphere into January is clearly unrealistic, and does not allow valid inferences to be drawn regarding ozone loss in that season.

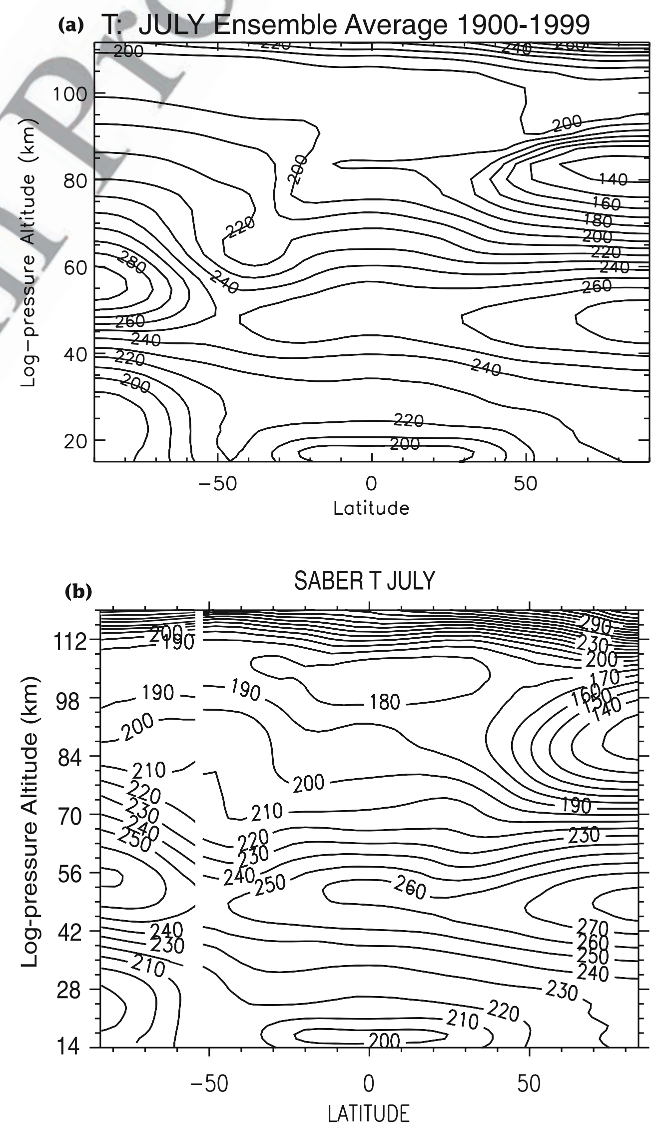


Figure 2. (a) Ensemble mean, zonal mean temperature (K) for July 1990–1999 from the WACCM3 simulations and (b) zonal mean temperature composite from SABER observations. SABER temperatures north of 52°S were obtained during the yaw period 1–19 July 2002; those south of 52°S, during the yaw period 19 July to 8 August 2005. See text for details.

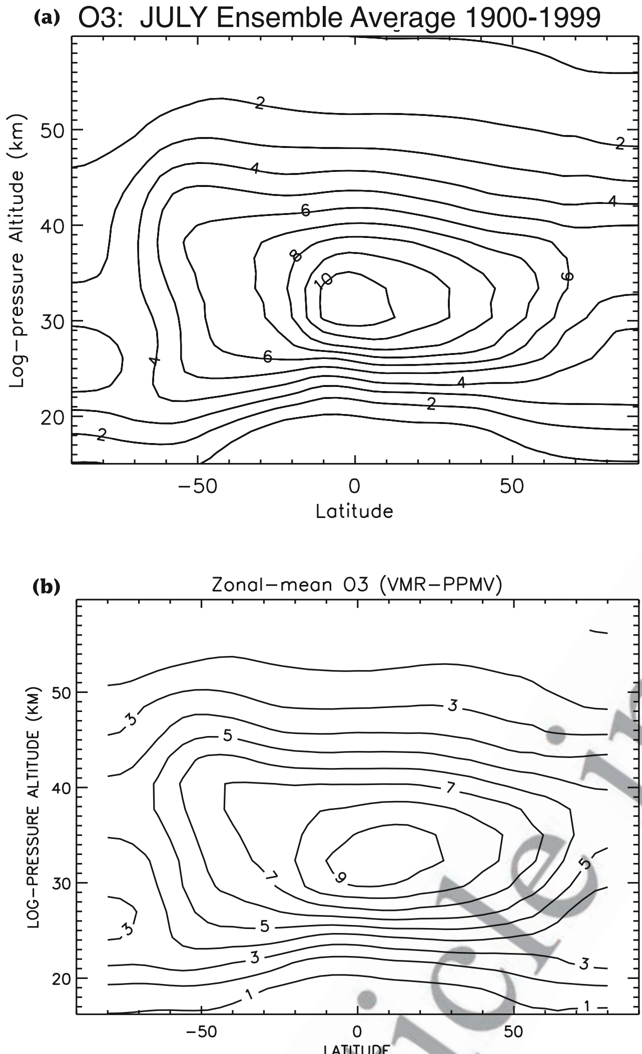


**Figure 3.** (a) Ensemble mean, zonal mean ozone (ppmv) for July 1990–1999 from the WACCM3 simulations and (b) zonal mean ozone from the URAP climatology. URAP ozone is derived from observations by the HALOE instrument. See text for details.



[33] Figure 2 shows the 1990s ensemble-average temperature field for July calculated with WACCM3 (Figure 2a), and a composite of temperature measurements made with the Sounding of the Atmosphere by Broadband Emission Radiometry (SABER) instrument onboard the Thermosphere-Ionosphere-Mesosphere Energetics and Dynamics (TIMED) spacecraft in 2002 and 2005 (Figure 2b). SABER coverage spans the range of latitude 52°S–83°N or 83°S–52°N, depending on the attitude of the spacecraft. Figure 2 shows SABER version 1.06 data mapped with *Salby*'s [1982] asynoptic Fourier transform technique for 1–19 July 2002 (52°S to 83°N) and for 19 July to 8 August 2005 (83°S to 54°S). The choice of these periods was based upon the availability at the time of this writing of version 1.06 with continuous coverage, suitable for asynoptic mapping [see *Garcia et al.*, 2005]. Note that since the SABER data come from a single year, they cannot be considered "climatological" values; nevertheless, the SABER data set is a unique standard of comparison because it provides a global view of the atmospheric temperature distribution from the tropopause to the lower thermosphere. Furthermore, the SABER temperature field shown in Figure 2b is in good qualitative and quantitative agreement with UKMO analyses for the 1990s [*Randel et al.*, 2004a, Figure 1] as regards the location and magnitude of the main features of the temperature distribution (Antarctic lower stratosphere, tropical cold point, summer and winter stratopause, summer mesosphere, etc.)

[34] The WACCM3 calculations reproduce the salient features of the temperature distribution over the wide range of altitude observed by SABER, with model-data differences generally less than 10 K. The main discrepancies occur at the summer mesopause, which is somewhat warm and slightly too low in WACCM3 compared with observations; at the "separated" winter stratopause, which is too warm in WACCM3; and at the summer stratopause, which is colder in WACCM3 than in SABER data. In the Antarctic lower stratosphere (~20 km) temperatures are about 5–7 K colder in WACCM3 than in SABER observations, comparable to the results obtained with other recent CCMs [*Austin et al.*, 2003]. Further, in the middle and upper stratosphere (1–10 mbar), model-data differences remain under 10 K, so the model does not exhibit the marked cold pole bias common to a number of other models compared by *Austin et al.* [2003]. On the other hand, as noted earlier in connection with the behavior of the zonal wind, Southern Hemisphere polar temperatures remain cold through Antarctic spring and early summer, so the cold bias with respect to observations in this region is actually more severe in October-December than it is in July.

[35] The 1990s ensemble average zonal mean ozone field for July computed with WACCM3 is shown in Figure 3a, while Figure 3b displays climatological data from URAP, which is based on observations by the Halogen Occultation Experiment (HALOE). The WACCM3 ensemble agrees in most respects with the HALOE data, except that the mixing ratio of ozone at the tropical maximum near 32 km is too high in WACCM3 by about 0.5 ppmv. *Eyring et al.* [2006] discuss this problem and note that it can be attributed to the mixing ratio of $NO_X$ being too low at the altitude of the ozone maximum in WACCM3 by about 15%.

[36] Finally, Figure 4 shows a comparison of the 1990s ensemble mean water vapor calculated with WACCM3 (Figure 4a) and the URAP climatology, which, as in the case of ozone, is based on HALOE observations. The major features of the observed water vapor distribution are well reproduced by WACCM3, although overall the mixing ratio is too low by about 0.5 ppmv, as a result of a small cold bias with respect to observations at the "cold point" tropical tropopause of the model, which determines the mixing ratio of air entering the stratosphere. WACCM3 simulates well the "tape recorder" [*Mote et al.*, 1996] behavior in the tropical lower stratosphere, both as regards amplitude and phase [see *Eyring et al.*, 2006]. The model also captures accurately the interhemispheric gradient of water vapor, which is the result of mean meridional transport. Note, for example, the region of enhanced water vapor over the south polar region at 5–10 mbar, a remnant of upper stratospheric, water-rich air from the previous Southern Hemisphere summer. Immediately below, there is a region of depleted

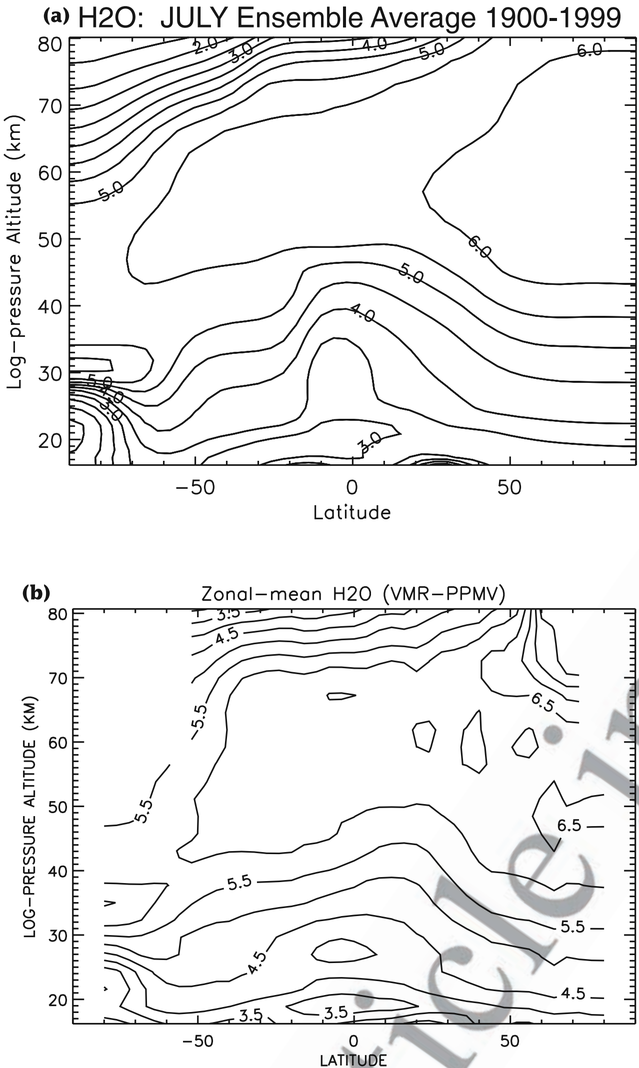


**Figure 4.** Same as Figure 3 except for water vapor.

water vapor, centered at 50 mbar, which is the result of dehydration due to cold temperatures in Antarctic winter (compare Figure 2). The behavior is more apparent in WACCM3 results because HALOE data are not available beyond 80°S.

## 4. Middle Atmosphere Trends

[37] In the following we discuss the trends in temperature, ozone and water vapor obtained from the WACCM3 simulations, and compare them whenever possible with those obtained from a variety of observations from ground-based instruments and satellite platforms. We also discuss changes in the strength of the stratospheric circulation based upon age of air calculations. Because global coverage for the stratosphere and lower mesosphere has only been available since 1979, comparisons with data focus on the last two decades of the 20th century and on the range of altitudes from the surface (or the tropopause) to the upper stratosphere. However, we also show "whole atmosphere" trends (surface to lower thermosphere) for the entire period of simulation, 1950–2003.

[38] Most trends are obtained from multiple regression of monthly and zonal mean, deseasonalized model fields onto time, $t$, and monthly mean 10.7 cm radio flux, f10.7.

$$y = a + bt + c\ \mathrm{f10.7}, \qquad (1)$$

where $y$ is the predicted field and the coefficient $b$ is the trend, usually expressed in K per decade for temperature, and either percent per year or percent per decade for water vapor. (All percentage trends are calculated with respect to the time mean value for the period over which the trend is computed.) This is essentially the same procedure used to determine trends from data, except that the multiple regressions from data often include an index of the quasi-biennial oscillation (QBO) as a predictor, something that is superfluous for WACCM3 since the model does not generate a QBO.

[39] For ozone, the regressions calculated from data and, in most cases, those obtained from WACCM3, substitute "effective equivalent stratospheric chlorine" (EESC) [*Fioletov and Shepherd*, 2005] in place of time in equation (1). Regression on EESC is motivated by the observation that the chlorine and bromine compounds that affect ozone have not changed linearly with time, except during the interval of steady growth from about 1975 to the early 1990s. Thus, in the case of ozone, the coefficient $b$ is no longer a trend in the usual sense, but a measure of the sensitivity of the predictand, $y$, to EESC (although, for simplicity, we refer to it as a trend below). In most instances, values of $b$ for WACCM3 are reported in units of ppmv of ozone per unit of EESC.

[40] Unless otherwise noted, all model trends are computed from monthly mean results averaged over the three model realizations, which enhances their statistical reliability.

### 4.1. Temperature

[41] Figure 5 shows zonal mean temperature trends for the stratosphere (K/decade) calculated from monthly mean

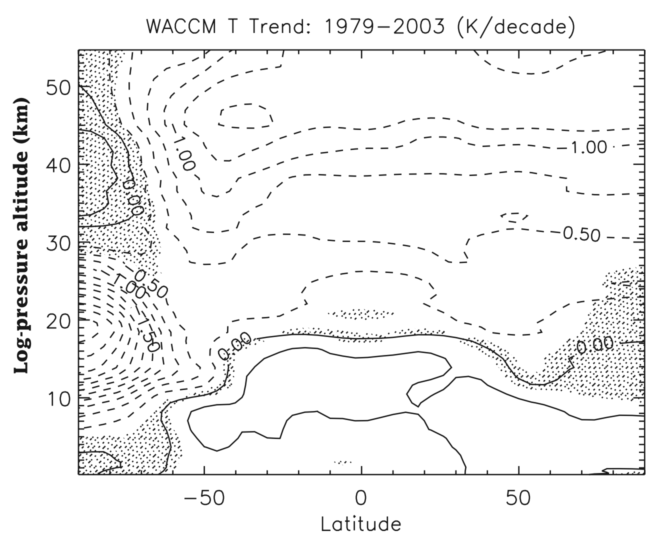


**Figure 5.** Zonal mean stratospheric temperature trend 1979–2003 (K/decade) calculated from the ensemble of WACCM3 realizations. Shaded regions denote trends that are not significant at the $2\sigma$ level.

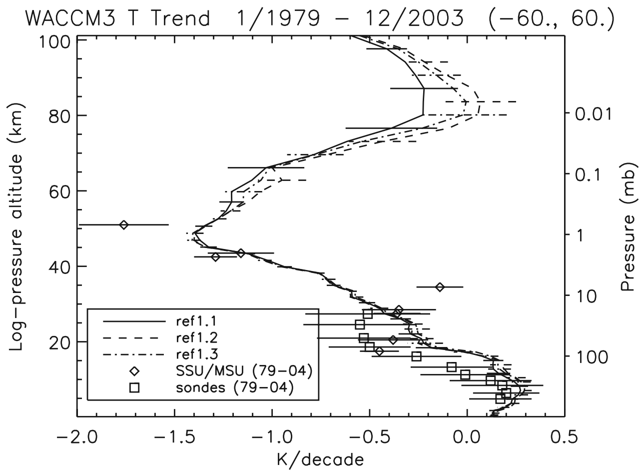


**Figure 6.** Zonal mean temperature trends (K/decade) averaged over $\pm 70^\circ$ for each member of the ensemble of WACCM3 simulations for the period 1979–2003 (solid, dashed, and dot-dashed curves) compared with similarly averaged trends for 1979–2004 derived from SSU/MSU observations (diamonds) and from radiosondes (squares). In all cases, the bars denote $2\sigma$ errors. See text for details.

WACCM3 output (Figure 5). The temperature trend is smallest near 70–100 mbar ($\sim$16–17 km) and increases with altitude up to about 1 mbar ($\sim$45 km), where it reaches values of $-1.25$ to $-1.50$ K/decade, with minor variations in latitude, except at high latitudes of the Southern Hemisphere. Over the southern polar cap the model computes a strong negative trend of more than $-2.5$ K/decade centered around 18–20 km, in the region of the ozone hole. In the Northern Hemisphere lower stratosphere, WACCM3 does not produce a significant temperature trend poleward of 70°. These results are broadly consistent with the CCM calculations of *Austin and Butchart* [2003] for the period 1980–1999, and with several of the models discussed by *Shine et al.* [2003]. However, they differ from observations [e.g., *Pawson and Naujokat*, 1999] and certain recent modeling results [e.g., *Lahoz*, 2000; *Braesicke and Pyle*, 2004; *Dameris et al.*, 2005] in that Arctic winters in the 1990s are not especially cold in the lower stratosphere, even though the model is driven by observed SSTs. The modeling studies cited suggest that specification of observed SSTs produces Arctic stratospheric temperatures that are cold in the 1990s, in agreement with observations. This behavior is not present in the WACCM3 simulations [cf. *Eyring et al.*, 2006, Figure 4], and contributes to the lack of a significant temperature trend in the Arctic lower stratosphere; it also has consequences for the calculated ozone trends in the Arctic, as discussed below.

[42] Figure 6 compares WACCM3 temperature trends for 1979–2003, averaged between 60°S and 60°N, with 1979–2004 trends computed from satellite data, and from radiosonde observations. The observed trends are obtained from linear regression upon time, omitting the two years after the volcanic eruptions of El Chichón and Mount Pinatubo. The model trends make no allowance for volcanic eruptions because heating by volcanic aerosols was not included in the simulations, as noted in section 2.8. The satellite observations are from the stratospheric sounding unit (SSU) for altitudes between about 20 km and the stratopause, and from the microwave sounding unit (MSU) channel 4 in the lowermost stratosphere. Radiosonde results are from a subset of stations between 60°S and 60°N, described by *Lanzante et al.* [2003] and updated as described by *Randel and Wu* [2006a]; this subset is chosen to omit stations with large artificial cooling biases, in particular those for which differences between MSU channel 4 and radiosonde trends are greater than 0.3 K/decade. WACCM3 trends are shown individually for each of the model realizations to illustrate the internal variability of the model. The $2\sigma$ error bars for the three model realizations overlap at all altitudes; differences with respect to SSU/MSU data are significant around 35 km ($\sim$6 mbar) and near the stratopause ($\sim$1 mbar). The reason for these discrepancies is not known. Trends calculated with other recent CCMs tend to bracket our results. For example, *Austin and Butchart* [2003] obtained global trends of about $-1.6$ K/decade at 1 mbar and $-0.8$ K/decade at 6 mbar for the period 1980–1999, which are similar to the results from WACCM3, whereas *Langematz et al.* [2003] calculated a trend for 1980–2000 of nearly $-2.5$ K/decade at 1 mbar, which is actually larger than the SSU/MSU trend. At mesospheric altitudes there are few observations to compare with WACCM3, but results from CCMs that extend beyond the stratosphere are generally consistent with those shown in Figure 6 [see, e.g., *Shine et al.*, 2003, Figure 4].

[43] Attribution of temperature trends to different factors (ozone decrease, increases in GHGs), as done for certain models by *Shine et al.* [2003], cannot be carried out with WACCM3 because the model has been run with interactive chemistry and radiation, which makes it impossible to separate the influences of each. However, calculations carried out with an earlier, noninteractive version of the model (not shown) yielded conclusions in line with those discussed by *Shine et al.* [2003], namely, that in the upper and lowermost stratosphere the cooling trend is dominated by the effect of ozone loss (see section 4.2), while in the middle stratosphere ($\sim$10 mbar) the effect of GHGs is most important.

[44] Figure 7 shows the temperature trend for the entire atmosphere up to 135 km calculated from the three model realizations for the entire period of simulation, 1950–2003. The morphology of the trend in the stratosphere is very similar to that of the trend shown in Figure 5, except that the magnitude is smaller. In the lower thermosphere (above 100 km) large trends are computed, peaking at $-2.5$ K/decade near 120 km. Interestingly, above that altitude the trends become smaller, which appears to be the result of the increasing dominance above about 125 km of IR cooling by the 5.3 $\mu$m emission of NO, a gas whose abundance remains essentially constant through the period 1950–2003. It bears repeating here that all model results, including those shown in Figure 7, are displayed in (isobaric) log pressure altitude. This should be kept in mind when comparing these results against observations made at geometric altitudes, especially in the thermosphere (above $\sim$100 km [see, e.g., *Akmaev and Fomichev*, 2000]).

[45] Near the mesopause, at 80–90 km, the calculated temperature trend is either insignificant or very small. The lack of a temperature trend in a range of altitude where $CO_2$

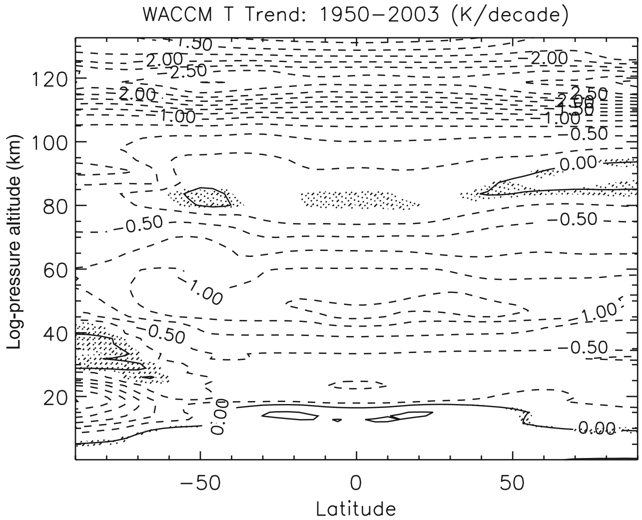


**Figure 7.** "Whole atmosphere" zonal mean temperature trend (K/decade) for 1950–2003 calculated from the ensemble of WACCM3 simulations. Shaded regions are not significant at the $2\sigma$ level.

is the main infrared emitter is puzzling, but appears to be consistent with available observations. For example, *Beig et al.* [2003] have compiled estimates of mesospheric temperature trends obtained from a variety of observations (ground-based, rocketsonde, satellite, etc.); they point out that the majority of the data sets examined, including the most reliable ones, show no significant temperature trend in this range of altitude. Note that the decrease in the geometric altitude of isobaric surfaces due to cooling of the atmosphere over the period 1950–2003 is less than 800 m near the mesopause, so temperature trends at 80–90 km would be essentially the same as shown in Figure 7 had they been calculated at constant geometric altitude.

[46] The reason for the lack of a temperature trend near the mesopause in the WACCM3 simulations is the subject of current investigation. However, *Schmidt et al.* [2006] have recently used the HAMMONIA CCM in a 2 × $CO_2$ experiment to show that the temperature change is small, and even statistically insignificant, at many locations near the mesopause. They attribute this behavior to compensating changes in dynamical heating by the mean meridional circulation. In contrast, *Manzini et al.* [2003] used the MAECHAM/CHEM model to perform time slice simulations for 1960 and 2000 conditions, and derived a temperature decrease between 1969 and 2000 of −4 K in the upper mesosphere, which is much larger than obtained by us or by Schmidt et al. This is perhaps due to the fact that the top boundary in MAECHAM/CHEM is located at 0.01 mbar, i.e., near the mean altitude of the mesopause, which may preclude compensating effects by the mean meridional circulation.

## 4.2. Ozone

[47] Figure 8 compares calculated ozone trends with results obtained from satellite measurements by the Stratospheric Aerosol and Gas Experiment (SAGE I and SAGE II), supplemented with ozonesonde observations at high latitudes [*Randel and Wu*, 2006b]. The observations are regressed upon ESSC, QBO, and solar cycle indices, whereas model results omit regression on the QBO, which is absent in WACCM3. The SAGE data cover the latitude range ±55°, from 20 to 50 km for SAGE I and from the tropopause to 50 km for SAGE II; ozonesonde observations are available in the polar regions at Syowa (69°S) and Resolute (75°N) from the tropopause to 30 km. Note therefore that the values shown in Figure 8b above 30 km in the polar regions are extrapolated from lower latitudes. Note also that the SAGE/ozonesonde results are expressed as the net change over the period 1979–2005, whereas WACCM3 trends with respect to EESC are computed for 1979–2003, since the simulations end in 2003. Finally, because WACCM3 results are expressed in percent change per unit of EESC, the values in Figure 8a should be multiplied times 1.5 (the change in EESC between 1979

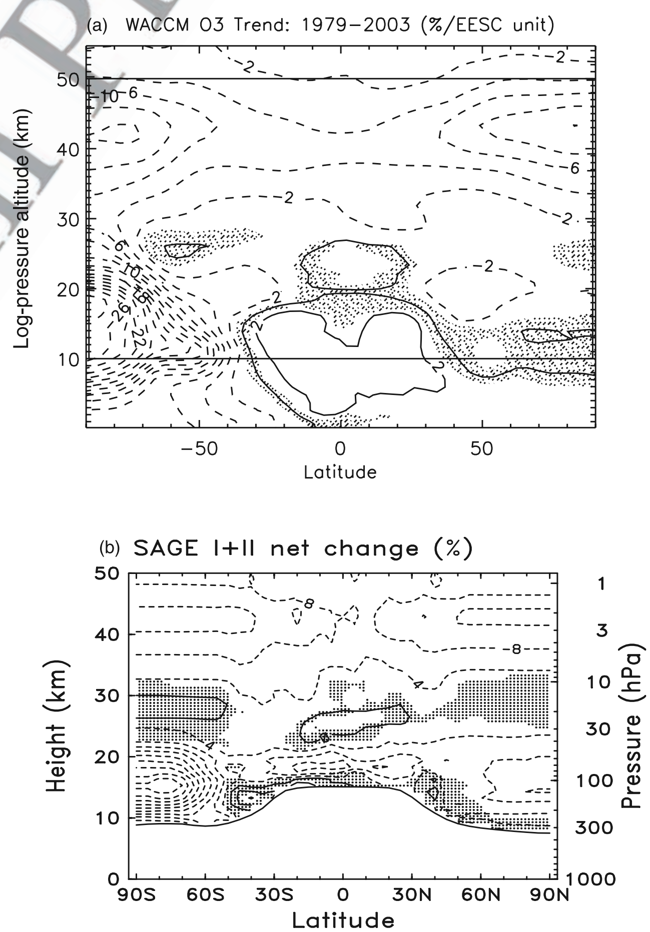


**Figure 8.** (a) Zonal mean ozone trend 1979–2003 (%/EESC unit) calculated from the ensemble of WACCM3 realizations and (b) percentage ozone change for the period 1979–2005 from SAGE I/II satellite observations (adapted from *Randel and Wu* [2006b]). The box inset in Figure 8a corresponds to the region covered by the data in Figure 8b; the values of Figure 8a should be multiplied times 1.5 (the change in EESC from 1979 to 2003) to compare them with those in Figure 8b. Shaded regions in Figures 8a and 8b denote trends that are not significant at the $2\sigma$ level. See text for details.

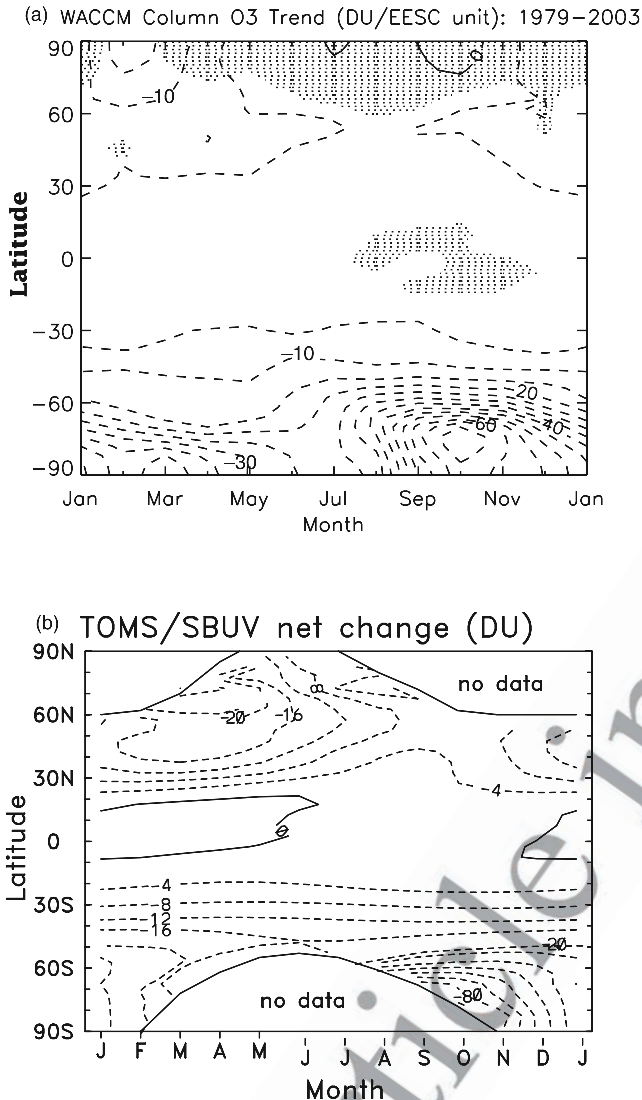


**Figure 9.** (a) Seasonal variation of the zonal mean ozone column trend, 1979–2003, calculated from the ensemble of WACCM3 simulations (DU/EESC unit) and (b) ozone column change (DU) from 1979 to 2005 derived from TOMS/SBUV data (adapted from *Randel and Wu* [2006b]). The values in Figure 9a should be multiplied times 1.5 to compare them with those in Figure 9b. Shaded regions in Figure 9a denote insignificant results at the $2\sigma$ level.

and 2003) in order to compare them with the SAGE/ozonesonde net changes shown in Figure 8b.

[48] Model results the observations are consistent in most regions of the stratosphere. Thus the largest ozone trends in the upper stratosphere are found around 40 km, and are about −8% per unit of EESC (or −12% change over the period 1979–2003), which agrees well with the change derived from the SAGE/ozonesonde data set. In both WACCM3 and the data there are regions of slight, albeit statistically insignificant, ozone increase in the tropics, at ~25 km and immediately above the tropopause, and a region of small trends between 25 and 30 km in extra-tropical latitudes whose significance is marginal. In the data there is region of strong negative trends in the tropics, centered near 18 km, which is not present in the WACCM3 results; however, as noted by *Randel and Wu* [2006b], SAGE trends in this region are of questionable validity.

[49] In the region of the ozone hole, WACCM3 calculates a maximum trend of −28% per unit of EESC at ~17 km (or −42% between 1979 and 2003, smaller than the −60% obtained from the Syowa ozonesonde data at ~15 km). On the other hand, negative trends over Antarctica extend throughout the stratosphere in WACCM, whereas those computed from the data are actually positive (although statistically insignificant) between 25 and 30 km. In the Arctic lower stratosphere, the discrepancy is larger: WACCM3 does not produce a significant trend, whereas the data indicate a net change of about −8%. This is consistent with the temperature results shown in Figure 5, where WACCM3 trends at high latitudes are insignificant poleward of 70°N. It is possible that observed trends in both temperature and ozone are influenced by the series of very cold Northern Hemisphere winters that occurred in the mid-1990s [cf. *Eyring et al.*, 2006, Figures 4 and 15], behavior that is not present in the WACCM3 results, as noted above. On average, WACCM3 zonal mean temperatures in the Northern Hemisphere polar cap in winter are warmer than observed by about 5 K, which can affect the efficiency of chlorine activation and, consequently, both ozone depletion and the trend thereof.

[50] Figure 9 compares results for the total ozone column as a function of season, with monthly mean resolution. The data are from the Total Ozone Mapping Spectrometer (TOMS) and the Solar Backscattered Ultraviolet (SBUV) satellite instruments for 1979–2005, as recently analyzed by *Randel and Wu* [2006b]. The ozone data are regressed upon ESSC, QBO, and solar cycle indices, and the results are expressed as net change in Dobson units (DU) over the period in question; WACCM3 results omit regression on the QBO, are shown in terms of DU per unit of EESC, and are computed for 1979–2003. As in Figure 8, the WACCM3 numbers should be multiplied by 1.5, the change in EESC between 1979 and 2003, in order to compare with the data.

[51] WACCM3 column trends are generally consistent with observations: They are small in the tropics and increase toward high latitudes, maximizing during the Northern and Southern Hemisphere spring seasons, when ozone depletion is largest. The model trends over the southern polar cap in October are −65 DU/EESC unit, or −97 DU over the period 1979–2003, very similar to what is obtained from the data for 1979–2005. Note, however, the persistence of large model ozone trends into January (−50%/EESC unit, or a change of −75% over 1979–2003), whereas the percentage change in the data drops rapidly after November, to about −30% in January. This is a manifestation of the cold bias that develops in the model during southern spring in the polar lower stratosphere, where temperatures remain cold and westerlies persist into January (see section 3).

[52] In the Northern Hemisphere, WACCM3 trends are considerably smaller than those observed; they are largest over the Arctic in February (−15 DU/EESC unit, or −22.5 DU for the period 1979–2003), but only −5 to −10 DU/EESC unit (−7.5 to −15 DU change from 1979 to 2003) poleward of 60°N in March, compared to as much as −20 DU at 60°N seen in the data for that month. Further, aside from the months of February and March, high-latitude

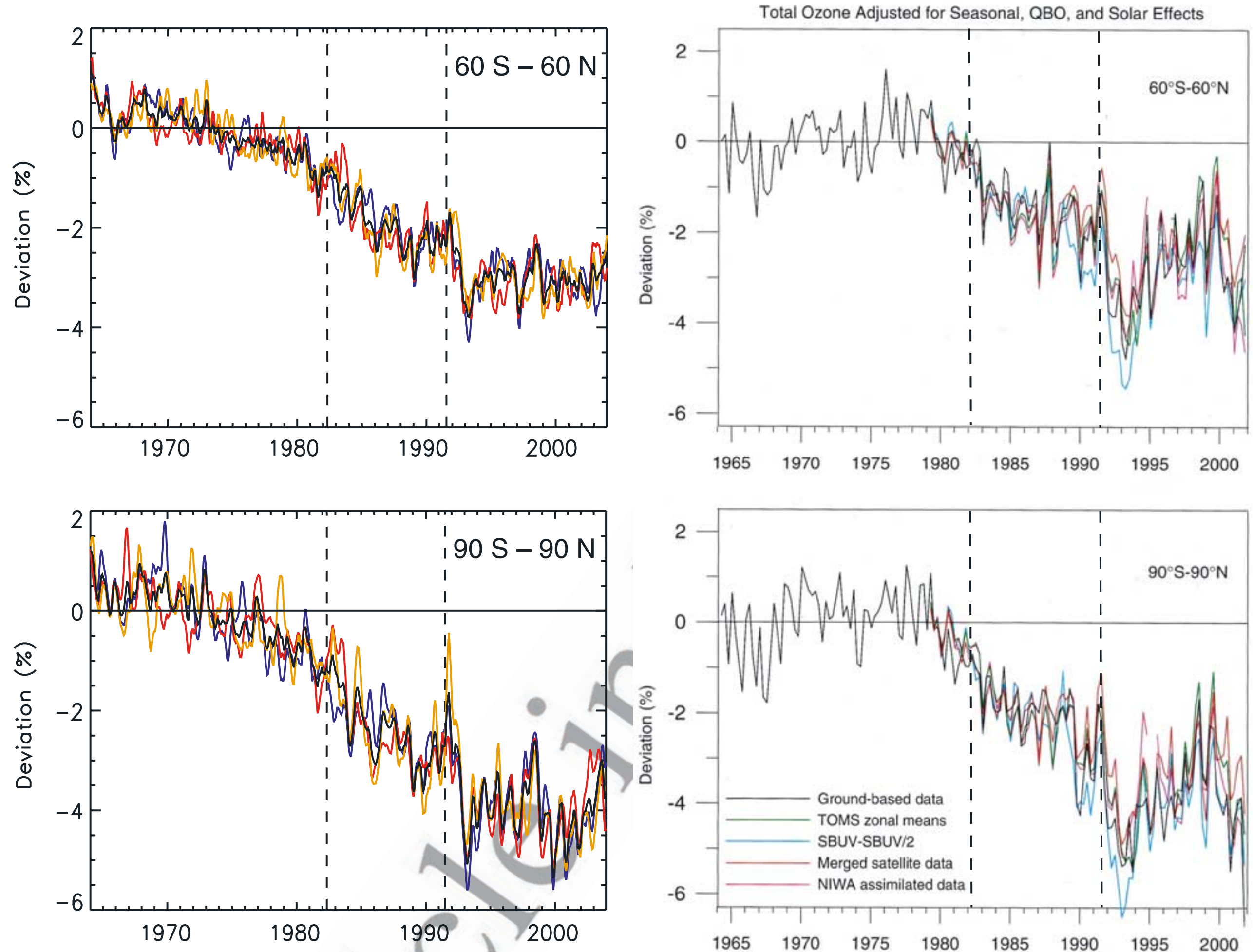


**Figure 10.** Evolution of zonal mean ozone column anomalies (percentage change averaged over ±60° and ±90°) for (left) each member of the WACCM3 ensemble compared with (right) the anomalies derived from various observational data sets (adapted from *WMO* [2003]). Both model results and data are smoothed with a 3-month running average, and the percentage anomalies are calculated with respect to the average column values for the period 1964–1980. The dashed lines denote the dates of the eruptions of El Chichón and Mount Pinatubo. See text for details.

trends in the Northern Hemisphere are very small (and statistically insignificant) in WACCM3, whereas the observed change remains larger than −8 DU throughout the entire period (April–July) when the satellite instruments are able to observe the northern polar cap. This is a reflection of the discrepancy between the ozone loss in the Arctic lower stratosphere calculated with WACCM3 and the larger observed loss, as noted in connection with Figure 8.

[53] The calculation of trends or net changes in ozone, as in Figures 8 and 9, provides a compact description of the evolution of ozone in the last few decades of the 20th century. However, because ozone changes in this period did not occur at a constant rate, it is useful to examine the secular evolution of the ozone column to see whether WACCM3 can capture the salient features of the observational record. Figure 10 shows the behavior of the ozone column anomaly since 1964 in WACCM3 and in observations, averaged between ±60° (Figure 10, top) and globally (Figure 10, bottom), as reported by *WMO* [2003]. In all cases the anomalies are calculated with respect to the mean ozone column for the period 1964–1980, as was done in the *WMO* [2003] Ozone Assessment [see also *Fioletov et al.*, 2002]. The data come from a variety of sources (TOMS, SBUV and ground-based instruments), and exhibit a high degree of consistency among data sets. For WACCM3, the results are shown for each of the three realizations and for their average. The dates of the eruptions of El Chichón and Mount Pinatubo are indicated in the plots.

[54] The evolution of the ozone column anomalies derived from WACCM3 agrees in most respects with the observations. In particular, the magnitude of the decrease is very similar for the globally averaged column (−5% in both cases), although slightly smaller in WACCM3 (−4%) than in the data (−4.5 to −5%) when averaged over ±60°. A sharp dip is seen in the model and the data after the eruption of Mount Pinatubo (June 1991), with column ozone reaching minimum values toward the end of 1992 whether averaged globally or over ±60°. This behavior has been

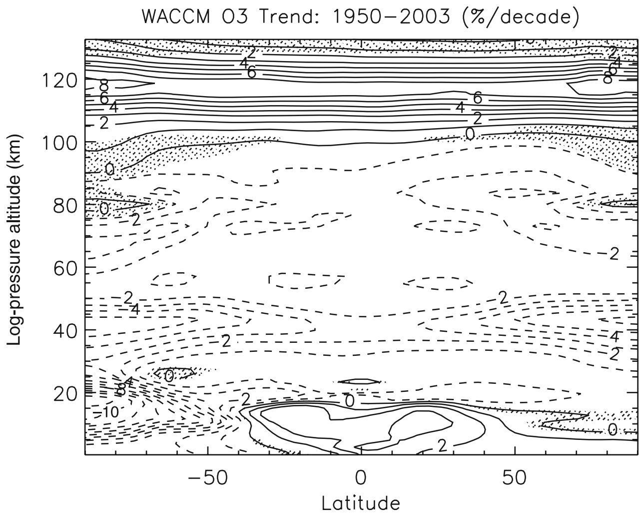


**Figure 11.** Same as Figure 7, except for ozone in units of percent change per decade.

attributed to the effect of the aerosol load introduced into the stratosphere by the eruption [*Brasseur and Granier*, 1992; *Hofmann et al.*, 1994]. Note, on the other hand, that there is little indication of a large column decrease after El Chichón (spring of 1982) in either the model or the observations. Note also that in both model and observations, ozone column anomalies show no consistent decrease in the period after about 1994. This is consistent with the fact that the value of EESC is nearly constant after 1994–1995, so no ozone change would be predicted by our ozone-EESC regression (Figure 8a). Whether this represents the beginning of ozone recovery cannot be answered definitively by the present calculations. However, WACCM3 calculations of the period 2000–2050, to be presented elsewhere, indicate that recovery, in the sense of a sustained increase in ozone column, does not begin until approximately 2005. Thus the behavior calculated (and observed) since the mid-1990s is perhaps best characterized as a "slowdown" of ozone loss [*Newchurch et al.*, 2003].

[55] The behavior of the global ozone column in one of the WACCM3 realizations, shown in gold in Figure 10, is remarkable in that the anomaly averaged over ±90° is almost zero in model year 1991 (the two other realizations have anomalies of about −2 to −3% with respect to the 1964–1980 average, which is typical of the early 1990s). This behavior is not seen in the column anomalies averaged over ±60°, which indicates it must be due to the contribution from the polar regions. Further examination reveals that the behavior can be isolated to the southern polar cap, where 1991 is a highly anomalous model year, with column ozone amounts in Antarctic spring (not shown) reaching values similar to those calculated for the 1960s and 1970s, before the development of the Antarctic ozone hole.

[56] The disappearance of the ozone hole in model year 1991 is reminiscent of the behavior observed in Antarctica in 2002, when a major stratospheric sudden warming virtually eliminated the ozone hole in September [see, e.g., *Charlton et al.*, 2005; *Hio and Yoden*, 2005; *Krüger et al.*, 2005; *Richter et al.*, 2005; *Roscoe et al.*, 2005; *Stolarski et al.*, 2005] However, the behavior in WACCM3 is different in several important respects: Disturbances of the Antarctic vortex due to large-amplitude planetary wave events occurred early in the winter season (as early as July) and several times thereafter; this prevented the normal development of cold temperatures, the activation of catalytic chlorine species, and the formation of the ozone hole. In addition, the zonal mean zonal wind, although exhibiting very large negative anomalies with respect to climatology (as much as $-55$ m s$^{-1}$), did not meet at any time during winter or spring the usual criterion for a major sudden warming (easterlies present at 10 mbar and 60°). These aspects of model year 1991 are similar to the Antarctic winter of 1988, as reported by *Kanzawa and Kaguchi* [1990] and *Hirota et al.* [1990], although that winter appears to have been somewhat less disturbed (large planetary wave events occurred later in the season, starting in August 1988 rather than in July, and they reduced but did not eliminate the ozone hole). A description of the unusual model year of 1991 will be presented elsewhere.

[57] Figure 11 shows the whole atmosphere ozone trend over the entire period of simulation, 1950–2003. Note that because the period shown begins well before the time of largest anthropogenic emissions of chlorine and bromine compounds, and because trends outside the stratosphere are due to factors others than chlorine/bromine catalysis of ozone, the results in Figure 11 are presented as actual temporal trends (in percent change per decade) rather than as changes per unit of EESC, as was done in Figures 8 and 9. In the troposphere, stratosphere and lower mesosphere the morphology of the trends is very similar to that obtained for 1979–2003 (Figure 8), although changes are smaller, reflecting the fact that the main factors that influence ozone, temperature and halogen abundance, have changed most rapidly in the last 2–3 decades of the 20th century. At higher altitudes, there is a negative trend up to ~100 km as a result of increasing water vapor (and hence $HO_X$, which dominates ozone destruction in the mesosphere); the water vapor increases are attributable, in the model, to increases in methane (as shown in section 4.3). In the lower thermosphere ozone actually increases (by as much as 6–8% per decade near 120 km), as a result of the large, negative temperature trend in this region (compare Figure 7). Finally, in the troposphere there is a net increase in ozone of about 2–3% per decade that can be attributed to increases in methane, whose oxidation leads to the production of ozone [*Crutzen*, 1973].

[58] As noted at the beginning of this section, WACCM3 trends for ozone are obtained from multiple regressions that include the 10.7 cm solar flux as a predictor, so it is appropriate to make note of the sensitivity displayed by WACCM3 to 11-year solar variability. Figure 12 shows the latitude dependence of the regression coefficient of column ozone on f10.7. At most latitudes the regression coefficient is between 2.5 and 3 DU per 100 units of f10.7. This is consistent with values derived from ground-based instruments and from BUV/SBUV satellite observations [*WMO*, 2003]; however, the values are substantially smaller than those obtained recently by *Stolarski et al.* [2006] using the Goddard Space Flight Center's chemistry transport model, and those derived by the same authors from combined TOMS/SBUV observations, which are about 4–6 DU per 100 units of f10.7 at most latitudes. The reason for this

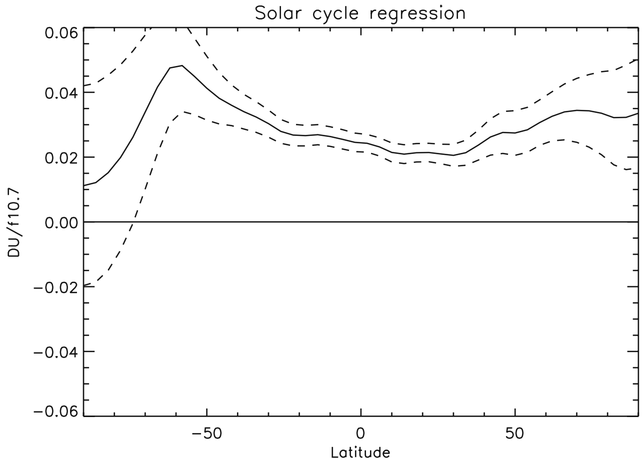


**Figure 12.** Latitude dependence of the solar cycle regression coefficient of column ozone on 10.7 cm solar flux (DU per unit of 10.7 cm flux). The regression is based on the ensemble of WACCM3 simulations for the period 1950–2003, which comprises five solar cycles. The dashed lines denote $2\sigma$ errors.

discrepancy is not clear, although it should be pointed out that the estimates shown in Figure 12 are based upon the entire 1950–2003 simulation period, whereas Stolarski et al.'s results are for 1979–2003; in addition Stolarski et al. also included volcanic aerosol loading as a predictor in their multiple regression, something that was not done in the WACCM3 analysis. It is also noteworthy that when regressions from WACCM3 output are calculated for the period 1979–2003, the regression coefficient for f10.7 (not shown) increases to about 4 DU per 100 units of f10.7.

### 4.3. Water Vapor

[59] While calculated temperature and ozone trends are generally consistent with observations, as shown in sections 4.1 and 4.2, this is not true of trends in water vapor, a constituent whose evolution has been carefully documented from hygrosonde observations made in Boulder, Colorado, over the last two decades, and in the satellite record provided by the HALOE instrument onboard UARS since 1992 [*Randel et al.*, 2004b]. Figure 13 shows a comparison of the trends calculated with WACCM3 (Figure 13a) and from HALOE data (Figure 13b) for the period 1992–2002. The latter are obtained from regression upon time and a QBO index, as explained by Randel et al. While HALOE shows declining water in the lower stratosphere together with strong increases (as much as 6% per decade) in the middle and upper stratosphere, WACCM3 trends are of the opposite sign in the lower stratosphere (2–4% per decade increases in the tropics), and positive but substantially smaller than HALOE trends in the middle and upper stratosphere.

[60] Agreement between model and observations is no better for the Boulder hygrosonde data, available since 1980 [*Oltmans et al.*, 2002], which are also computed from regression upon time and QBO index and are shown in Figure 14. These observations have been cited in recent works as evidence that stratospheric water vapor is undergoing a rapid increase (as much as 10% per decade), which may imply significant changes in tropical tropopause temperatures, or even dynamics [see, e.g., *Randel et al.*, 2004b]. Comparison with WACCM3 trends over 1992–2002 shows that the latter are about one half, or even less, of those derived from the Boulder hygrosondes. Further, model trends are rather variable among the three realizations, which are shown separately in Figure 14. Also shown in Figure 14 is the 1992–2002 trend at the latitude of Boulder derived from HALOE data; this trend does not agree with either the hygrosondes or the model and, indeed, it is of the opposite sign below about 23 km.

[61] While it is possible that water vapor has indeed undergone large secular changes over the last 10–20 years, an alternative interpretation of the results shown in Figures 13 and 14 is that trends calculated over decadal timescales are unstable; that is, they are not indicative of long-term change but instead reflect the presence of low-frequency

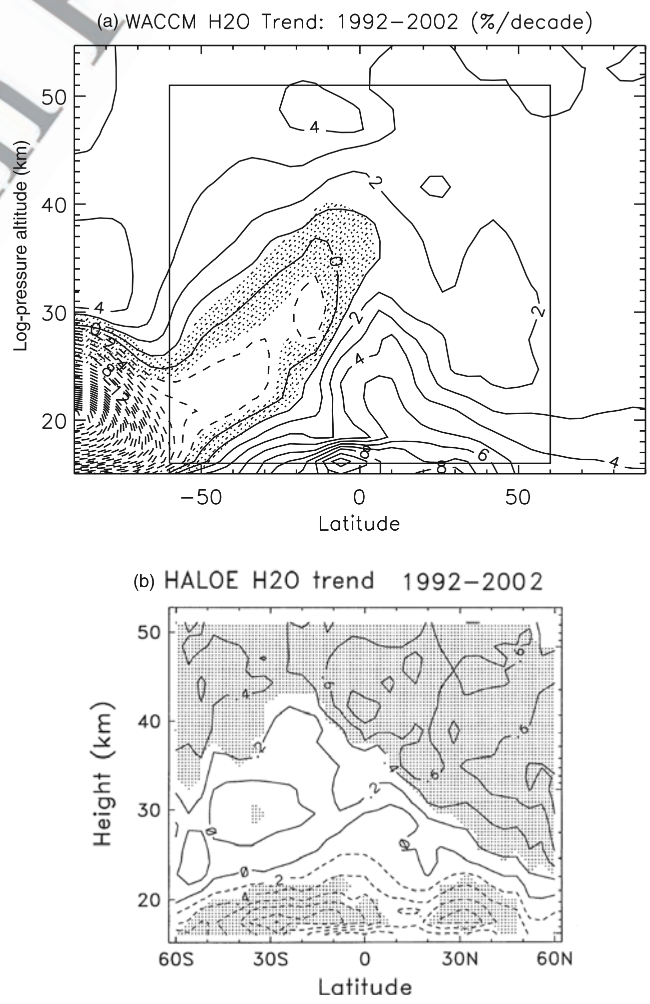


**Figure 13.** (a) Zonal mean water vapor trend 1992–2002 (percent per decade) calculated from the ensemble of WACCM3 realizations; (b) the trend (percent per year) calculated from HALOE observations (adapted from *Randel et al.* [2004b]). Shaded regions in Figure 13a denote trends that are not significant at the $2\sigma$ level; in Figure 13b, the shading denotes significance at the $2\sigma$ level.

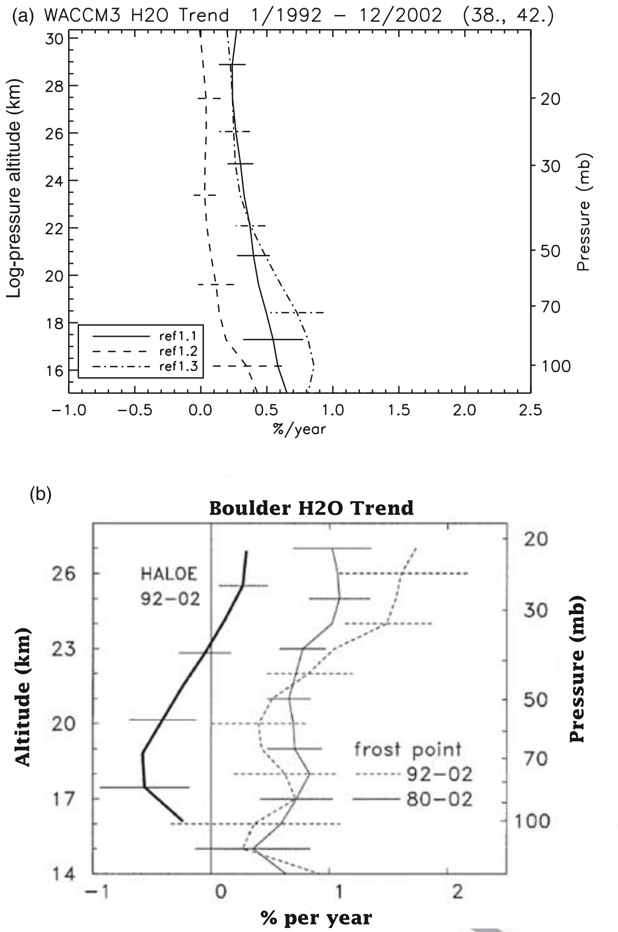


**Figure 14.** (a) Zonal mean water vapor trend (percent per year) as a function of altitude for each member of the WACCM3 ensemble averaged over (38–42°N) for 1992–2002 and (b) zonal mean trend at 40°N calculated from HALOE data (1992–2002, heavy solid line) and local trends from Boulder (40°N) hygrosonde data (1980–2002, light solid line; and 1992–2002, dashed line); all adapted from *Randel et al.* [2004b]. Bars denote $2\sigma$ errors.

variability inherent in the behavior of water vapor. Such variability can resemble a trend, even a statistically significant one, but may disappear when a sufficiently long time series is analyzed. In support of this interpretation Figure 15 shows WACCM3 trends computed for two arbitrary 10-year periods, 1975–1985 and 1980–1990. In the first period, trends are positive throughout most of the stratosphere and exceed 6% per decade in certain regions; in the second, trends are substantially smaller in the upper stratosphere, and negative in the lower stratosphere. Only over Antarctica, where water vapor abundance is strongly influenced by dehydration associated with the ozone hole, are the trends similar between the two periods shown in Figure 15. It is clear that the trends in either simulation cannot be representative of long-term behavior but instead must reflect the influence of low-frequency variability.

[62] For the WACCM3 simulations, it is necessary to compute trends over three or more decades in order to obtain stable results. When WACCM3 trends are calculated for the entire period of simulation 1950–2003, as shown in Figure 16, a stable pattern emerges in the stratosphere and mesosphere, where the long-term trend can be attributed to the increase in methane between 1950 and 2003 (about 0.6 ppmv, which implies an increase of 1.2 ppmv in water vapor, sufficient to account for the maximum 4% per decade trend in water vapor seen in the upper stratosphere and mesosphere). In addition, a negative trend is calculated over Antarctica even in this long record, indicative of the growth of the ozone hole (and thus of colder temperatures) in the last 20 years; and a positive trend is calculated in the troposphere, as a result of the increase in relative humidity allowed by the small but significant tropospheric temperature trend due to the greenhouse effect (compare Figure 7).

[63] These results raise the question what are the sources of low-frequency variability in the behavior of water vapor in the middle atmosphere. Because water vapor in the middle atmosphere is very strongly influenced by the temperature of the entry region at the tropical cold point tropopause, it is to be expected that any processes that affect

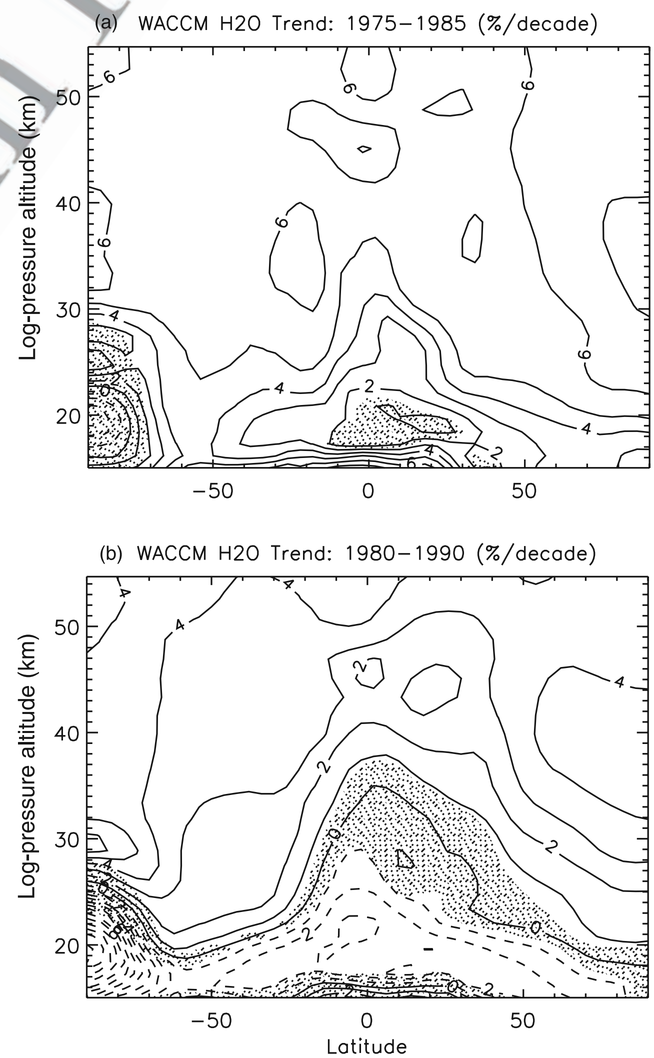


**Figure 15.** Zonal mean water vapor trends (percent per decade) calculated from the WACCM3 ensemble for two arbitrary 10-year periods: (a) 1975–1985 and (b) 1980–1990. Shading denotes insignificant trends at the $2\sigma$ level.

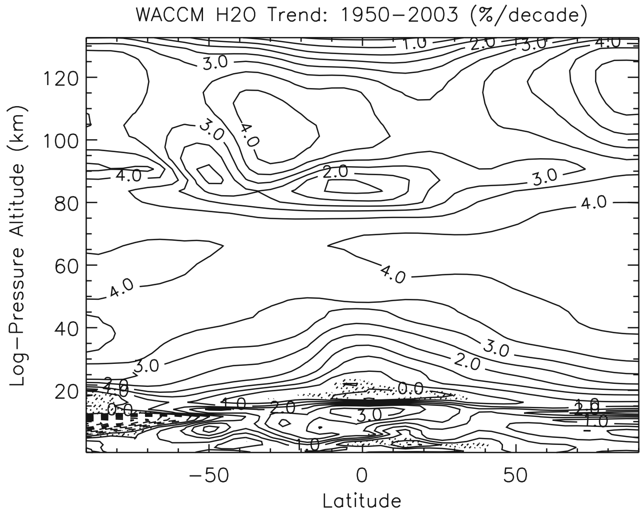


**Figure 16.** Same as Figure 7, except for water vapor in units of percent per decade.

the cold point temperature will exert a strong influence on water vapor abundance. The most obvious such processes that operate on timescales of several years are the QBO (through the adiabatic effect of downwelling and upwelling associated with the QBO secondary circulation) [*Plumb and Bell*, 1982; *Giorgetta and Bengtsson*, 1999; *Randel et al.*, 2004b]; volcanic eruptions (which heat the tropopause region when solar radiation is absorbed by volcanic aerosols) [*Stenchikov et al.*, 2002; *Joshi and Shine*, 2003]; and El Niño–Southern Oscillation (ENSO, which modifies upper tropospheric and lower stratospheric temperatures) [*Geller et al.*, 2002; *Calvo Fernández et al.*, 2004; *Fueglistaler and Haynes*, 2005].

[64] The effect of ENSO on the simulation of water vapor in WACCM3 is illustrated in Figure 17, which shows the behavior of water vapor anomalies in the tropics from 1950 to 2003 (Figure 17a), and their correlation with the Niño-3.4 (N3.4) index as a function of altitude and time lag (Figure 17b). N3.4 is a conventional indicator of ENSO intensity based upon sea surface temperature anomalies in the region 170°W–120°W, 5°S–5°N. It is clear from Figure 17a that enhanced water vapor in the troposphere often accompanies the occurrence of ENSO events, and this is followed by an increase in the lowermost stratosphere that propagates upward at the speed of the tropical "tape recorder." Figure 17b shows that this effect is reflected in the lag correlation between water vapor anomalies and N3.4, which is as large as 0.7 in the troposphere a few months after the maximum of N3.4; in the stratosphere the correlation maximizes at lags that increase with time (as expected from transport), and reach values between ±0.2 and ±0.4. These results are consistent with those of *Scaife et al.* [2003], who documented the impact of ENSO events on stratospheric water vapor using the UK Met's Unified Model.

[65] Because WACCM3 does not generate a QBO, and because heating by volcanic aerosols was not included in the present simulations, it is not surprising that short-term water vapor trends, such as those shown in Figures 13 and 14,



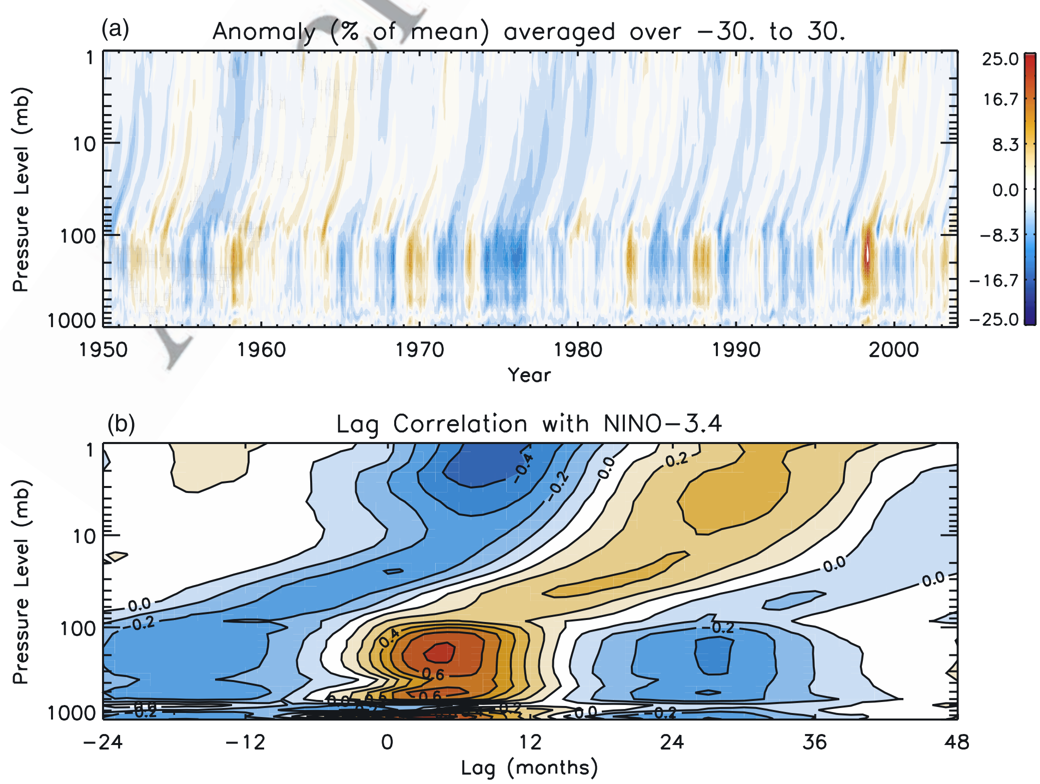


**Figure 17.** (a) Water vapor anomalies (percentage deviation from the time mean) calculated from the WACCM3 ensemble for the period 1950–2003 and (b) lag correlation coefficient of the anomalies shown in Figure 17a with the N3.4 ENSO index. See text for details.

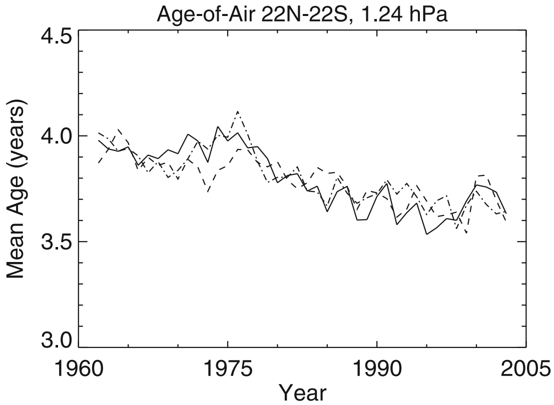


**Figure 18.** Evolution of the age of air between 1963 and 2003 at 1.2 mbar, averaged over ±22°, for each of the members of the WACCM3 ensemble.

do not agree with observations. It also appears that successful simulation of observed water vapor trends will require at a minimum the inclusion of a realistic QBO and aerosol heating rates in addition to ENSO effects. Even then, it may be necessary to examine trends over perhaps as long as three decades before an unambiguous attribution can be made, a conclusion consistent with the findings of *Fueglistaler and Haynes* [2005]. Finally, it is also apparent that the trends derived from HALOE and shown in Figure 14, which represent a zonal mean at the latitude of Boulder, cannot be reconciled with the local hygrosonde data. This suggests that the behavior of water in the lower stratosphere over Boulder may be influenced by local processes not captured in the HALOE observations, or that there are unknown errors in one or both sets of observations.

### 4.4. Stratospheric Age of Air

[66] The stratospheric age of air (AOA) is a measure of the strength of the stratospheric circulation obtained by comparing the mixing ratio of a steadily increasing "age of air tracer" at some reference point to the mixing ratio elsewhere in the stratosphere. The reference point is usually chosen to be in the upper tropical troposphere, in the vicinity of the entry region of air into the global stratosphere [see *Hall and Plumb*, 1994; *Hall et al.*, 1999]. Specifically, the AOA may be defined as

$$\tau_A(y,z) = t_\chi(y,z) - t_\chi(y_0,z_0), \qquad (2)$$

where $t_\chi(y, z)$ is the time at which a certain mixing ratio, $\chi$, of the AOA tracer is reached at some location ($x$, $y$) in the meridional plane, and $t_\chi(y_0, z_0)$ is the (earlier) time when the same mixing ratio occurs at the reference point ($x_0$, $y_0$). AOA is determined from observations of long-lived, steadily increasing trace gases with sinks present only at very high altitudes, like $CO_2$ or $SF_6$. In WACCM3 we use an ad hoc, conservative AOA tracer whose concentration increases linearly in time with a constant surface flux.

[67] Figure 18 shows the evolution of $\tau_A$(1 mbar), averaged over ±22 ° for each of the three WACCM3 realizations. Note that AOA is only shown starting in 1963 because the tracer is initialized to zero everywhere in the model domain at the start of each simulation and, as a consequence, it takes about a dozen years before its mixing ratio throughout the meridional plane equilibrates to values representative of the AOA. The results are remarkably consistent among the realizations and indicate that in the 40 years displayed in Figure 18, $\tau_A$(1 mbar) decreases by about 4 months, from a little under 4 years to a bit more than 3.5 years, or about 8.25% with respect to its initial value.

[68] The strengthening of the stratospheric (Brewer-Dobson) circulation in response to increases in GHGs has been documented previously by *Hansen et al.* [2005], who compared an ensemble of General Circulation models. Similar results for AOA have been obtained by *Austin and Li* [2006] with the AMTRAC model of the Geophysical Fluid Dynamics Laboratory, although in that model the decrease of AOA from 1960 to 2005 at 1 mbar (averaged between ±20°) is about 8 months, about twice the value than we obtain. This would seem to imply a more sensitive response of the global circulation to climate change in the last half of the 20th century in AMTRAC compared to WACCM3, the reasons for which remain moot at this time. In any case, we show below that the AOA change in WACCM3 is consistent with the trend in tropical upwelling.

[69] Figure 19 shows the trend in the tropical average (±22°) of the zonal mean vertical velocity as a function of altitude for the combined ensemble of WACCM3 simulations, along with individual time series at selected levels. We use the conventional Eulerian zonal mean, $\overline{w}$, which is not expected to be significantly different from the Transformed Eulerian mean in the tropics [*Andrews et al.*, 1987]. The model results have been smoothed with a 12-month running mean to remove short-term variability and emphasize the secular behavior. The WACCM3 ensemble of $\overline{w}$ shows significant positive trends at all altitudes between 15 and 50 km; typical values between 20 and 35 km are a bit less than $5\times10^{-6}$ m s$^{-1}$ per decade, with somewhat larger values near the tropopause and a much larger increase between 40 and 45 km. (In all cases, these trends are <10% of the time mean at the corresponding altitude.) A very simple test of consistency between these results and the AOA changes shown in Figure 18 can be carried out as follows: Ignoring lateral mixing in the "tropical pipe" region [*Plumb*, 1996] near the equator, we assume that the AOA at some distance, $\Delta Z$, above the tropopause is given approximately by the traveltime,

$$\tau = \frac{\Delta Z}{\overline{w}}, \qquad (3)$$

so that

$$\delta\tau = -\frac{\Delta Z}{\overline{w}^2}\,\delta\overline{w} = -\frac{\tau^2}{\Delta Z}\,\delta\overline{w}. \qquad (4)$$

At 1 mbar (∼45 km), the distance above the tropopause is $\Delta Z \sim 30$ km, while $\delta\,\overline{w} \sim 2\times10^{-5}$ m s$^{-1}$, or about 2 m d$^{-1}$. The last number is arrived at by taking an estimate of $0.5\times10^{-6}$ m s$^{-1}$ per decade as representative of the long-term trend in $\overline{w}$ throughout much of the stratosphere and multiplying times 4 decades (the period over which the AOA shown in Figure 18 is computed). With these

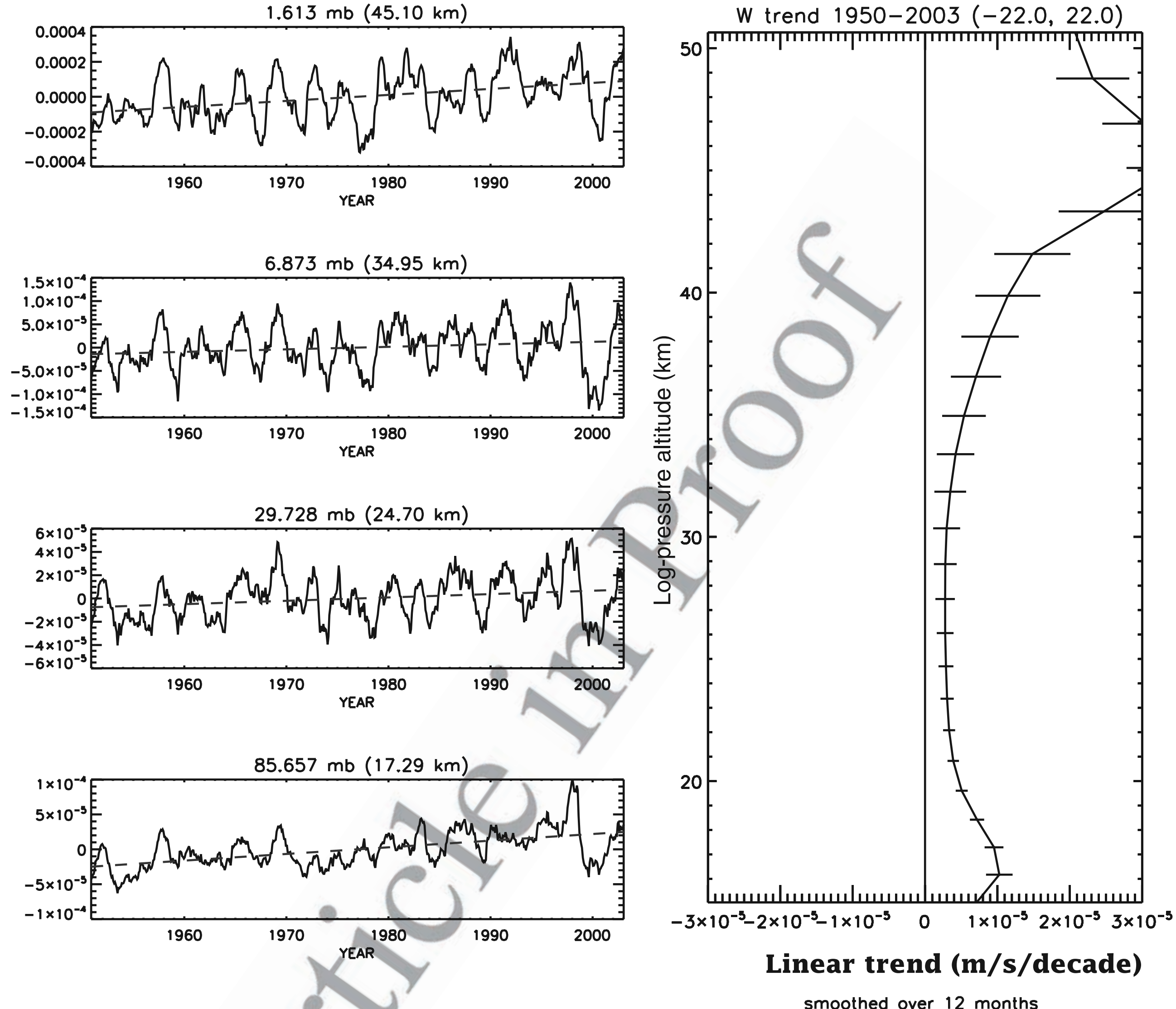




**Figure 19.** (left) Ensemble average time series of the zonal mean vertical velocity, $\overline{w}$, averaged over 22°N–22°S calculated with WACCM3 at selected altitudes. (right) Vertical profile of the ensemble average trend in $\overline{w}$ (m s$^{-1}$ per decade). Bars in Figure 19 (right) denote $2\sigma$ errors.

numbers, and a value of $\tau$(1 mbar) ~4 years, or about 1400 days, we have from (4)

$$\delta\tau = -\frac{(1400 \text{ days})^2}{3 \times 10^4 \text{ m}} \times 2 \text{ m d}^{-1} \sim -130 \text{ days}, \qquad (5)$$

which is consistent with the 4 month decrease in AOA seen in Figure 19. This result, which is also consistent with the findings of *Austin and Li* [2006], suggests that the decrease in AOA can indeed be interpreted as a strengthening of the global circulation insofar as the tropical average of $\overline{w}$ is a measure of the global upwelling in the stratosphere.

[70] One might ask whether such changes in the global stratospheric circulation play a role in the secular trends calculated by WACCM3. A simple way to approach the question is to ask how changes in the flux of trace species due to an enhancement of the circulation compare to changes induced by other processes, in particular by trends in the tropospheric mixing ratio of the tracer in question. If the tropical average of the advective flux of $\chi$ entering the stratosphere is given by

$$F = \overline{w}\,\overline{\chi}, \qquad (6)$$

then fractional changes in the flux may be expressed as

$$\frac{\delta F}{F} = \frac{\delta\overline{w}}{\overline{w}} + \frac{\delta\overline{\chi}}{\overline{\chi}}. \qquad (7)$$

In WACCM3, the fractional change attributable to changes in tropical upwelling, $\delta\overline{w}/\overline{w}$, is less than 0.1, while the fractional change due to changes in mixing ratio, $\delta\overline{\chi}/\overline{\chi}$, can be quite large over the period 1950–2003 for CFCs and other halogens; even for methane and $CO_2$, $\delta\overline{\chi}/\overline{\chi}$ has values of 0.5 and 0.2, respectively. Thus it appears that the strengthening of the stratospheric circulation documented in Figure 19 plays a minor role in altering the stratospheric abundance of trace gases whose tropospheric sources have undergone large changes in the period of simulation.

[71] There remains the question whether changes of 5–10% in the strength of tropical upwelling might influence temperatures in the tropical cold point region and therefore the water vapor mixing ratio of air entering the stratosphere. According to Figure 19, the net change in $\overline{w}$ at the tropical tropopause over the period 1950–2003 is $\sim 5 \times 10^{-5}$ m s$^{-1}$. From the thermodynamic equation one can estimate the change in temperature implied by a change in vertical velocity as

$$\delta\overline{T} \simeq -\frac{\Gamma}{\alpha}\,\delta\overline{w}. \qquad (8)$$

Using values $\alpha = 0.01$ d$^{-1}$ [*Randel et al.*, 2001] for the radiative relaxation rate and $\Gamma = 2$ K km$^{-1}$ for the lapse rate in the upper tropical troposphere in equation (7) gives $\delta\,T = -1$ K. However, the temperature trends over 1950–2003, shown in Figure 7, do not indicate a temperature change at the model's cold point (85 mbar, or $\sim$17 km) nearly as large as this. The model cold point temperature change between 1950 and 2003 averaged over ±22 ° is smaller than −0.25 K, and its statistical significance is marginal. Similarly, water vapor trends in the lower stratosphere (Figure 16) do not indicate a change commensurate with a 1 K decline in temperature (the average water vapor change over the period 1950–2003, averaged over ±22 is nearly zero, and statistically insignificant in any case). This suggests that other processes (e.g., changes in the radiative budget due to changes in GHGs, or changes in tropical convection) overwhelm the impact of changes in tropical upwelling on the cold point temperature (and hence on the water vapor mixing ratio of air entering the stratosphere) in the WACCM3 calculations.

## 5. Conclusions

[72] An ensemble of three simulations of the period 1950–2003 was carried out with NCAR's Whole Atmosphere Community Climate Model (WACCM3) in order to determine whether this new coupled chemistry-climate model is able to reproduce accurately the changes in the composition and temperature of the middle atmosphere brought about by anthropogenic emissions of GHG and halogenated compounds. Boundary conditions followed, for the most part, the recommendations of *Eyring et al.* [2005, 2006], as explained in section 2.8. Our results may be summarized as follows:

[73] 1. WACCM3 results are consistent with the observed trends for temperature and ozone over the last two decades of the 20th century, when satellite observations allow the estimation of such trends as functions of latitude and altitude throughout the stratosphere and lower mesosphere. The model agrees with observations both as regards the magnitude of the trends and their morphology in the latitude/height plane. The main discrepancies between modeled and observed trends include a smaller than observed temperature trend near 50 km; smaller calculated ozone loss than observed in Arctic spring; and ozone losses over Antarctica that persist into January. While there is no clear explanation for the smaller than observed upper stratospheric temperature trend computed with WACCM3, discrepancies in the polar lower stratosphere may be traced to deficiencies in the model's dynamical climatology, which is too warm in Arctic winter, and produces cold temperatures and westerly winds that persist too long in Antarctic spring.

[74] 2. Additional findings of interest in the WACCM3 simulations include a region of small, statistically insignificant temperature trends near the mesopause (80–85 km), and the occurrence of one highly disturbed Southern Hemisphere winter when the Antarctic ozone hole did not develop. The lack of a temperature trend near the mesopause is consistent with the majority of observations for this altitude range, as recently reviewed by *Beig et al.* [2003]; the mechanism that leads to this lack of response is the subject of current study. As regards the Antarctic ozone hole, we find that the southern winter of 1991 (a single case out of the 162 years of simulation in our three-member ensemble), is so disturbed by strong planetary wave events that the conditions necessary for chlorine activation are absent during most of the season. The behavior is reminiscent of observations during 2002, although in that Antarctic winter there was substantial ozone depletion early on, which was removed later by the major sudden warming of September 2002. Another important difference between model year 1991 and the observations for 2002 is that in the model, the zonal mean zonal wind is never reversed at 10 mbar and 60°S, so a major warming never occurs according to this conventional criterion. In this regard, model year 1991 resembles the behavior observed in 1988, which was characterized by several major disturbances throughout the winter season, but no wind reversal at 10 mbar and 60°S.

[75] 3. In contrast with the broad agreement found for ozone and temperature, water vapor trends are not at all consistent with the best available observational data sets: the HALOE satellite measurements since 1992 and the Boulder hygrosonde observations, which are available since 1980. Calculated trends do not reproduce the morphology, the magnitude or, at certain locations, even the sign of the observed trends. However, we show that such lack of agreement is to be expected when trends are calculated over relatively short periods of 10–20 years because water vapor is subject to sources of low-frequency variability that can masquerade as trends. In WACCM3, the most important source of low-frequency variability is ENSO, which introduces large anomalies in the mixing ratio of water vapor entering the stratosphere; the QBO and heating due to volcanic aerosols are other sources of low-frequency variability that will have to be included in future calculations in order to understand the observed variability of water vapor. In any case, when model trends are computed over the entire period of simulation, 1950–2003, the only secular trend that emerges is that due to the increase of methane, which accounts for the maximum calculated water vapor trend of 4% per decade in the upper stratosphere and mesosphere.

[76] 4. We have also documented trends in the model's age of air, which becomes progressively younger through the period of simulation. At 1 mbar in the tropics, AOA is

just under 4 years in 1963, decreasing to 3.6–3.7 years by 2003. We show that this decrease is consistent with a slight increase in the strength of tropical upwelling. The increase in tropical upwelling, which is about 5–10% of the time mean upwelling for the period, plays a minor role in altering the flux into the stratosphere of species whose mixing ratios have strong anthropogenic trends (halogenated compounds, methane, and even $CO_2$). On the other hand, a change in upwelling of 5–10% at the tropical cold point tropopause would imply a temperature change of as much as −1 K over 1950–2003, given the very long radiative lifetime in this region. However, the calculated temperature change at the model's cold point (85 mbar) is just −0.25 K, and is only marginally significant, which suggests that other processes, such as changes in the radiative budget due to changes in GHGs, or changes in tropical convection, overwhelm the effect of changes in upwelling.

[77] Taken together, our results show that a state-of-the-art CCM such as WACCM3 is able to simulate faithfully most changes in middle atmosphere composition and temperature structure over the last 50 years, a necessary condition for the use of such models to assess climate change and ozone recovery in the 21st century. Comparisons of model results against observations also point out deficiencies in the model's climatology that need to be corrected in order to improve the simulation of ozone loss in the polar lower stratosphere. Finally, the ensemble of WACCM3 simulations has revealed some poorly understood facets of the response of the middle atmosphere to anthropogenic change, such as the lack of temperature trends near the mesopause, the rare occurrence of an extremely disturbed Southern Hemisphere winter, and systematic changes in age of air, that suggest potentially fruitful topics for further study.

## Appendix A: Gravity Wave Parameterization

[78] Vertically propagating gravity waves are excited in the atmosphere when stably stratified air flows over an irregular lower boundary, and also by internal heating and shear. WACCM3 incorporates a gravity wave parameterization that solves separately for a general spectrum of monochromatic waves and for a single stationary wave generated by flow over orography.

[79] Vertically propagating gravity waves are excited in the atmosphere when stably stratified air flows over an irregular lower boundary, and also by internal heating and shear. WACCM3 incorporates a gravity wave parameterization that solves separately for a general spectrum of monochromatic waves and for a single stationary wave generated by flow over orography.

### A1. Adiabatic Inviscid Formulation

[80] Following *Lindzen* [1981], the equations for the gravity wave parameterization are obtained from the linearized two-dimensional hydrostatic momentum, continuity and thermodynamic equations in a vertical plane. Assuming a solution of the form

$$w'(Z,t) = \hat{w}\ e^{ik(x-ct)}\ e^{Z/2H}, \tag{A1}$$

where $Z$ is log pressure altitude, $H$ is the scale height, $k$ is the horizontal wave number and $c$ is the phase speed of the wave, leads to the wave equation

$$\frac{d^2\hat{w}}{dZ^2} + \lambda^2\hat{w} = 0, \tag{A2}$$

where

$$\lambda = \frac{N}{(U-c)}, \tag{A3}$$

$U$ is the background wind, and $N$ is the buoyancy frequency. The WKB solution of (A2) is

$$\hat{w}(Z) = A\ \lambda^{-1/2}\exp\left(i\int_0^Z \lambda dz'\right), \tag{A4}$$

and the full solution, from (A1), is

$$w'(Z,t) = A\lambda^{-1/2}\exp\left(i\int_0^Z \lambda dz'\right)\ e^{ik(x-ct)}\ e^{Z/2H}. \tag{A5}$$

The constant $A$ is determined from the wave amplitude at the source ($Z = 0$). The Reynolds stress associated with (A5) is

$$\tau(Z) \equiv -\rho\overline{u'w'} = \tau(0) = \frac{1}{2k}\ |A|^2\rho_0\ \mathrm{sgn}(\lambda_0) \tag{A6}$$

and is conserved (independent of $Z$), while the momentum flux $\overline{u'w'} = -(m/k)\ \overline{w'w'}$ grows exponentially with height as $\exp(Z/H)$, per (A5). We note that the vertical flux of wave energy is $c_{gz}E' = (U - c)\ \tau$ [*Andrews et al.*, 1987], where $c_{gz}$ is the vertical group velocity, so that deposition of wave momentum into the mean flow will be accompanied by a transfer of energy to the background state (see section A5).

### A2. Saturation Condition and Momentum Deposition

[81] The wave amplitude in (A5) grows as $e^{Z/2H}$ until the wave becomes unstable. At that point, the amplitude is assumed to be limited to the magnitude that would lead to the onset of instability, and the wave is said to be "saturated." The saturation condition used is taken from *McFarlane* [1987], and is based on a maximum Froude number, $F_c$, or streamline slope:

$$|\rho\overline{u'w'}| \le |\tau^*| = F_c^2\ \rho\frac{k\ |U-c|^3}{2\ N}, \tag{A7}$$

where $\tau^*$ is the saturation stress. In WACCM3 $F_c^2 = 1$ and is omitted hereafter. Following *Lindzen* [1981], within a saturated region the momentum tendency can be determined analytically from the divergence of $\tau^*$:

$$\frac{\partial U}{\partial t} = e\frac{1}{\rho}\frac{\partial\tau^*}{\partial Z}\ \simeq -e\ \frac{k(U-c)^3}{2NH}, \tag{A8}$$

where $e$ is an "efficiency factor," which represents the temporal and spatial intermittency in the wave sources. The analytic solution (A8) is not used in WACCM3; it is shown here to illustrate how the acceleration due to breaking gravity waves depends on the intrinsic phase speed. In the model the stress, which is conserved except where limited by saturation (A7) or by thermal damping and molecular diffusion (see section A3), is computed at the model layer interfaces and differenced to obtain the specific force at the layer midpoints.

### A3. Diffusive and Radiative Damping

[82] In addition to breaking as a result of instability, vertically propagating waves can also be damped by molecular diffusion (both thermal and momentum) or by radiative cooling. We take into account the molecular viscosity, $K_m$, and parameterize the radiative cooling with a Newtonian cooling coefficient, $\alpha$. The stress profile is then given by

$$\tau(Z) = \tau(Z_0)\exp\left(-\frac{2}{H}\int_{Z_0}^{Z}\lambda_i dz'\right), \tag{A9}$$

where $Z_0$ denotes the top of the region, below $Z$, not affected by thermal dissipation or molecular diffusion. The imaginary part of the local vertical wave number, $\lambda_i$ is

$$\lambda_i = \frac{N}{2k(U-c)^2}\left[\alpha + \frac{N^2}{(U-c)^2}\,K_m\right]. \tag{A10}$$

In WACCM3, (A9) and (A10) are only used within the molecular diffusion domain (above ~75 km). Below that altitude, molecular diffusion is negligible and radiative damping is also weak, so (A10) reduces to $\lambda_i \simeq 0$ and $\tau$ is conserved outside of saturation regions.

### A4. Transport Due to Dissipating Waves

[83] When the wave is dissipated, either through saturation or diffusive damping, there is a transfer of wave momentum and energy to the background state. In addition, a phase shift is introduced between the wave's vertical velocity field and its temperature and constituent perturbations so that fluxes of heat and constituents are nonzero within the dissipation region. The nature of the phase shift and the resulting transport depends on the dissipation mechanism; in WACCM3, we assume that the dissipation can be represented by a linear damping on the potential temperature and constituent perturbations. For potential temperature, $\theta$, this leads to

$$\left(\frac{\partial}{\partial t} + U\frac{\partial}{\partial x}\right)\theta' + w'\frac{\partial\bar{\theta}}{\partial z} = -\delta\theta', \tag{A11}$$

where $\delta$ is the dissipation rate implied by wave breaking, which depends on the wave's group velocity, $c_{gz}$ [*Garcia*, 1991]:

$$\delta = \frac{c_{gz}}{2H} = k\,\frac{(U-c)^2}{2HN}. \tag{A12}$$

Substitution of (A12) into (A11) then yields the eddy heat flux:

$$\overline{w'\theta'} = -\left[\frac{\delta\,\overline{w'w'}}{k^2(U-c)^2+\delta^2}\right]\frac{\partial\bar{\theta}}{\partial z}. \tag{A13}$$

Similar expressions can be derived for the flux of chemical constituents, with mixing ratio substituted in place of potential temperature in (A13). We note that these wave fluxes are always down gradient and that for convenience of solution, they may be represented as vertical diffusion, with coefficient $K_{zz}$ equal to the term in brackets in (A13), but they do not represent turbulent diffusive fluxes but rather eddy fluxes. Any additional turbulent fluxes due to wave breaking are ignored. To take into account the effect of localization of turbulence [e.g., *Fritts and Dunkerton*, 1985; *McIntyre*, 1989], (A13) is multiplied times an inverse Prandtl number, $Pr^{-1}$; in WACCM3 we use $Pr^{-1} = 0.25$.

### A5. Heating Due to Wave Dissipation

[84] The vertical flux of wave energy density, $E'$, is related to the stress according to

$$c_{gz}\,E' = (U-c)\,\tau, \tag{A14}$$

where $c_{gz}$ is the vertical group velocity [*Andrews et al.*, 1987]. Therefore the stress divergence $\partial\tau/\partial Z$ that accompanies wave breaking implies a loss of wave energy. The rate of dissipation of wave energy density is

$$\frac{\partial E'}{\partial t} \simeq (U-c)\frac{1}{c_{gz}}\frac{\partial\tau}{\partial t} = (U-c)\frac{\partial\tau}{\partial Z}. \tag{A15}$$

For a saturated wave, the stress divergence is given by (A8), so that

$$\frac{\partial E'}{\partial t} = (U-c)\,\frac{\partial\tau^*}{\partial Z} = -e\rho\,\frac{k\,(U-c)^4}{2NH}. \tag{A16}$$

This energy loss by the wave represents a heat source for the background state, as does the change in the background kinetic energy density implied by wave drag on the background flow:

$$\frac{\partial\overline{K}}{\partial t} \equiv \frac{\rho}{2}\frac{\partial U^2}{\partial t} = U\,\frac{\partial\tau^*}{\partial Z} = -e\rho\,\frac{k\,U\,(U-c)^3}{2NH}, \tag{A17}$$

which follows directly from (A8). The background heating rate, in K s$^{-1}$, is then

$$Q_{gw} = -\frac{1}{\rho\,c_p}\left[\frac{\partial\overline{K}}{\partial t} + \frac{\partial E'}{\partial t}\right]. \tag{A18}$$

Using (A16)–(A17), this heating rate may be expressed as

$$Q_{gw} = \frac{1}{\rho\,c_p}\,c\,\frac{\partial\tau^*}{\partial Z} = \frac{1}{c_p}\left[e\frac{k\,c\,(c-U)^3}{2NH}\right], \tag{A19}$$

where $c_p$ is the specific heat at constant pressure. In WACCM3, $Q_{gw}$ is calculated for each component of the gravity wave spectrum using the first equality in (A19), i.e., the product of the phase velocity times the stress divergence.

## A6. Orographic Source Function

[85] For orographically generated waves, the source is taken from *McFarlane* [1987]:

$$\tau_0 = |\rho\overline{u'w'}|_0 = \frac{k}{2}\ h_0^2\ \rho_0 N_0 U_0, \tag{A20}$$

where $h_0$ is the streamline displacement at the source level, and $\rho_0$, $N_0$, and $\overline{u}_0$ are also defined at the source level. For orographic waves, the subgrid-scale standard deviation of the orography $\sigma$ is used to estimate the average mountain height, determining the typical streamline displacement. The source level quantities $\rho_0$, $N_0$, and $U_0$ are defined by vertical averages over the source region, taken to be $2\sigma$, the depth to which the average mountain penetrates into the domain. The source level wind vector determines the orientation of the coordinate system used in the WKB solution and the magnitude of the source wind $U_0$.

## A7. Gravity Wave Spectrum Source

[86] A gravity wave spectrum is also included in WACCM3. The wave source is assumed to be located at the first interface above 500 mbar and to be oriented in the direction of the wind on that interface. At all higher levels, the local wind vector is projected onto the source wind vector $\mathbf{U}_s$, reducing the problem to two dimensions. The source stress spectrum is specified as a Gaussian in phase speed,

$$\tau_s(c) = \tau_b \exp\left[-\left(\frac{c - U_s}{c_w}\right)^2\right], \tag{A21}$$

centered on the source wind, $U_s = |\mathbf{U}_s|$, with width $c_w$ = 30 m s$^{-1}$. The phase speed spectrum is also centered on $U_s$ and a range of phase speeds with specified width and resolution is used:

$$c \in U_s + [\pm\Delta c, \pm 2\Delta c, .. \pm c_{\max}]. \tag{A22}$$

In WACCM3, we use $\Delta c$ = 2.5 m s$^{-1}$ and $c_{\max}$ = 80 m s$^{-1}$, giving 64 phase speeds. Above the source region, the saturation condition (A7) is enforced separately for each phase speed.

[87] The source spectrum is a function of latitude and time of year, specified as

$$\tau_b = \tau_b^*\ F(\phi, t), \tag{A23}$$

where $\tau_b^*$ is a constant and $F(\phi, t)$ is a function intended to represent the seasonal and latitudinal variation of the source spectrum, following the results of *Charron and Manzini* [2002]:

$$F(\phi, t) = \max\left(0.1,\ F_\phi^N F_t^N + F_\phi^S F_t^S\right). \tag{A24}$$

The Northern and Southern Hemisphere latitude functions are

$$F_\phi^{N,S} = \frac{1}{2}\left[1 + \tanh\left(\pm\frac{\phi \mp \phi_0}{d_0}\right)\right] \exp\left[-\left(\frac{\phi \mp \phi_1}{d_1}\right)^2\right], \tag{A25}$$

where $\phi_0 = 20°$, $d_0 = 10°$, $\phi_1 = 60°$, and $d_1 = 50°$; and the time functions are

$$F_t^{N,S} = c_1^{N,S} \pm c_2^{N,S} \cos\left(\frac{2\pi d_y}{365}\right), \tag{A26}$$

where $0 \leq d_y < 365$ is the day of the year. The constants used when the model is run at 4° × 5° resolution are $c_1^N = 1$, $c_2^N = 0.4$, $c_1^S = 1.2$ and $c_2^N = 0.2$.

[88] The value of $\tau_b^*$ is perhaps the most important "adjustable parameter" in the gravity wave source spectrum. In practice, $\tau_b^*$ is adjusted so as to reverse the stratospheric summer easterly and winter westerly jets at an altitude consistent with observations, and to produce a cold summer mesopause also consistent with observations. At the 4° × 5° resolution used in this study, we take $\tau_b^* = 6 \times 10^{-3}$ Pa.

[89] **Acknowledgments.** We wish to thank S. Walters for his work implementing and testing the WACCM3 code, without which this study would not have been possible, and W. J. Rande, A. K. Smith, and three anonymous reviewers for their comments on the original manuscript. The National Center for Atmospheric Research is sponsored by the U.S. National Science Foundation. Most of the calculations for this study were carried out on the Columbia system of the NASA Advanced Supercomputing Facility, Ames Research Center, California.

## References


Akmaev, R. A., and V. I. Fomichev (2000), A model estimate of cooling in the mesosphere and lower thermosphere due to the $CO_2$ increase over the last 3–4 decades, *Geophys. Res. Lett.*, *27*, 2113–2116.

Andrews, D. G., J. R. Holton, and C. B. Leovy (1987), *Middle Atmosphere Dynamics*, 489 pp., Elsevier, New York.

Austin, J., and N. Butchart (2003), Coupled chemistry-climate model simulations for the period 1980 to 2020: Ozone depletion and the start of ozone recovery, *Q. J. R. Meteorol. Soc.*, *129*, 3225–3249.

Austin, J., and F. Li (2006), On the relationship between the strength of the Brewer-Dobson circulation and the age of stratospheric air, *Geophys. Res. Lett.*, *33*, L17807, doi:10.1029/2006GL026867.

Austin, J., et al. (2003), Uncertainties and assessments of chemistry-climate models of the stratosphere, *Atmos. Chem. Phys.*, *3*, 1–27.

Banks, P. M., and G. Kockarts (1973), *Aeronomy, Part B*, 355 pp., Elsevier, New York.

Barth, C. A., K. D. Mankoff, S. M. Bailey, and S. C. Solomon (2003), Global observations of nitric oxide in the thermosphere, *J. Geophys. Res.*, *108*(A1), 1027, doi:10.1029/2002JA009458.

Beig, G., et al. (2003), Review of mesospheric temperature trends, *Rev. Geophys.*, *41*(4), 1015, doi:10.1029/2002RG000121.

Braesicke, P., and J. A. Pyle (2004), Sensitivity of dynamics and ozone to different representations of SSTs in the unified model, *Q. J. R. Meteorol. Soc.*, *130*, 2033–2045.

Brasseur, G. P., and C. Granier (1992), Impact of heterogeneous chemistry on model predictions of ozone changes, *J. Geophys. Res.*, *97*, 18,015–18,033.

Brasseur, G. P., D. A. Hauglustaine, S. Walters, P. J. Rasch, J.-F. Muller, C. Granier, and X.-X. Tie (1998), MOZART: A global chemical transport model for ozone and related chemical tracers, Part 1: Model description, *J. Geophys. Res.*, *103*, 28,265–28,289.

Briegleb, B. P. (1992), Delta-Eddington approximation for solar radiation in the NCAR Community Climate Model, *J. Geophys. Res.*, *97*, 7603–7612.

Calvo Fernández, N., R. R. Garcia, R. García Herrera, D. Gallego Puyol, L. Gimeno Presa, E. Hernández Martín, and P. Ribera Rodríguez (2004), Analysis of the ENSO signal in tropospheric and stratospheric temperatures observed by MSU, 1979–2000, *J. Clim.*, *17*, 3934–3946.

Charlton, A. J., A. O'Neill, W. A. Lahoz, and P. Berrisford (2005), The splitting of the stratospheric polar vortex in the Southern Hemisphere, September 2002: Dynamical evolution, *J. Atmos. Sci.*, *62*, 590–602.

Charron, M., and E. Manzini (2002), Gravity waves from fronts: Parameterization and middle atmosphere response in a general circulation model, *J. Atmos. Sci.*, *59*, 923–941.

Collins, W. D., J. K. Hackney, and D. P. Edwards (2002), An updated parameterization for infrared emission and absorption by water vapor in the National Center for Atmospheric Research Community Atmosphere Model, *J. Geophys. Res.*, *107*(D22), 4664, doi:10.1029/2001JD001365.

Collins, W. D., et al. (2004), *Description of the NCAR Community Atmosphere Model (CAM3)*, Natl. Center for Atmos. Res., Boulder, Colo.

Considine, D. B., A. R. Douglass, P. S. Connell, D. E. Kinnison, and D. A. Rottman (2000), A polar stratospheric cloud parameterization for the global modeling initiative three-dimensional model and its response to stratospheric aircraft, *J. Geophys. Res.*, *105*, 3955–3973.

Crutzen, P. J. (1973), A discussion of the chemistry of some minor constituents in the stratosphere and troposphere, *Pure Appl. Geophys.*, *106–108*, 1385–1399.

Dameris, M., et al. (2005), Long-term changes and variability in a transient simulation with a chemistry-climate model employing realistic forcing, *Atmos. Chem. Phys.*, *5*, 2121–2145.

Dickinson, R. E., E. C. Ridley, and R. G. Roble (1981), A three-dimensional general circulation model of the thermosphere, *J. Geophys. Res.*, *86*, 1499–1512.

Eyring, V., D. E. Kinnison, and T. G. Shepherd (2005), Overview of planned coupled chemistry-climate simulations to support upcoming ozone and climate assessments, *SPARC Newslett.*, *25*, 11–17.

Eyring, V., et al. (2006), Assessment of coupled chemistry-climate models: Evaluation of dynamics, transport characteristics and ozone, *J. Geophys. Res.*, in press.

Fioletov, V. E., and T. G. Shepherd (2005), Summertime total ozone variations over middle and polar latitudes, *Geophys. Res. Lett.*, *32*, L04807, doi:10.1029/2004GL022080.

Fioletov, V. E., G. E. Bodeker, A. J. Miller, R. D. McPeters, and R. Stolarski (2002), Global and zonal total ozone variations estimated from ground-based and satellite measurements: 1964–2000, *J. Geophys. Res.*, *107*(D22), 4647, doi:10.1029/2001JD001350.

Fomichev, V. I., J. P. Blanchet, and D. S. Turner (1998), Matrix parameterization for the 15 $\mu$m $CO_2$ band cooling in the middle and upper atmosphere for variable $CO_2$ concentration, *J. Geophys. Res.*, *103*, 11,505–11,528.

Friedl, R. (Ed.) (1997), Atmospheric effects of subsonic aircraft: Interim assessment report of the advanced subsonic technology program, *NASA Ref. Publ., 1400*, 143 pp.

Fritts, D. C., and T. J. Dunkerton (1985), Fluxes of heat and constituents due to convectively unstable gravity waves, *J. Atmos. Sci.*, *42*, 549–556.

Froehlich, C. (2000), Observations of irradiance variations, *Space Sci. Rev.*, *94*, 15–24.

Fueglistaler, S., and P. H. Haynes (2005), Control of interannual and longer-term variability of stratospheric water vapor, *J. Geophys. Res.*, *110*, D24108, doi:10.1029/2005JD006019.

Garcia, R. R. (1991), Parameterization of planetary wave breaking in the middle atmosphere, *J. Atmos. Sci.*, *48*, 1405–1419.

Garcia, R. R., and B. A. Boville (1994), "Downward control" of the mean meridional circulation and temperature distribution of the polar winter stratosphere, *J. Atmos. Sci.*, *51*, 2238–2245.

Garcia, R. R., and S. Solomon (1985), The effect of breaking gravity waves on the dynamics and chemical composition of the mesosphere and lower thermosphere, *J. Atmos. Sci.*, *90*, 3850–3868.

Garcia, R. R., R. Lieberman, J. M. Russell, and M. G. Mlynczak (2005), Large-scale waves in the mesosphere and lower thermosphere observed by SABER, *J. Atmos. Sci.*, *62*, 4384–4399.

Geller, M. A., X. Zhou, and M. Zhang (2002), Simulations of the interannual variability of stratospheric water vapor, *J. Atmos. Sci.*, *59*, 1076–1085.

Giorgetta, M. A., and L. Bengtsson (1999), Potential role of the quasi-biennial oscillation in the stratosphere-troposphere exchange as found in water vapor in general circulation model experiments, *J. Geophys. Res.*, *104*, 6003–6019.

Hall, T. M., and R. A. Plumb (1994), Age as a diagnostic of stratospheric transport, *J. Geophys. Res.*, *99*, 1059–1070.

Hall, T. M., D. W. Waugh, K. A. Boering, and A. R. Plumb (1999), Evaluation of transport in stratospheric models, *J. Geophys. Res.*, *104*, 18,815–18,839.

Hansen, J., et al. (2005), Efficacy of climate forcings, *J. Geophys. Res.*, *110*, D18104, doi:10.1029/2005JD005776.

Hauglustaine, D. A., G. P. Brasseur, S. Walters, P. J. Rasch, J.-F. Mller, L. K. Emmons, and M. A. Carroll (1998), MOZART: A global chemical transport model for ozone and related chemical tracers: 2. Model results and evaluation, *J. Geophys. Res.*, *103*, 28,291–28,335.

Hedin, A. E. (1987), MSIS-86 thermospheric model, *J. Geophys. Res.*, *92*, 4649–4662.

Hedin, A. E. (1991), Extension of the MSIS thermosphere model into the middle and lower atmosphere, *J. Geophys. Res.*, *96*, 1159–1172.

Hio, Y., and S. Yoden (2005), Interannual variations of the seasonal march in the Southern Hemisphere stratosphere for 1979–2002 and characterization of the unprecedented year 2002, *J. Atmos. Sci.*, *62*, 567–580.

Hirota, I., K. Kuroi, and M. Shiotani (1990), Midwinter warmings in the Southern Hemisphere stratosphere in 1988, *Q. J. R. Meteorol. Soc.*, *116*, 929–941.

Hofmann, D. J., S. J. Oltmans, J. A. Lathrop, J. M. Harris, and H. Voemel (1994), Record low ozone at the South Pole in the spring of 1993, *Geophys. Res. Lett.*, *21*, 421–424.

Holton, J. R. (1982), The role of gravity wave-induced drag and diffusion in the momentum budget of the mesosphere, *J. Atmos. Sci.*, *39*, 791–799.

Horowitz, L. W., et al. (2003), A global simulation of tropospheric ozone and related tracers: Description and evaluation of MOZART, version 2, *J. Geophys. Res.*, *108*(D24), 4784, doi:10.1029/2002JD002853.

Hurrell, J. W., J. J. Hack, A. S. Phillips, J. Caron, and J. Yin (2006), The dynamical simulation of the Community Atmosphere Model version 3 (CAM3), *J. Clim.*, *19*, 2162–2183.

Intergovernmental Panel on Climate Change (IPCC) (2001), *Climate Change 2001: The Scientific Basis. Contributions of Working Group 1 to the Third Assessment Report of the Intergovernmental Panel on Climate Change*, edited by J. T. Houghton et al., 881 pp., Cambridge Univ. Press, New York.

Joshi, M. M., and K. P. Shine (2003), A GCM study of volcanic eruptions as a cause of increased stratospheric water vapor, *J. Clim.*, *16*, 3525–3534.

Kanzawa, H., and S. Kawaguchi (1990), Large stratospheric sudden warming in Antarctic late winter and shallow ozone hole in 1988, *Geophys. Res. Lett.*, *17*, 77–80.

Kiehl, J. T., and B. P. Briegleb (1991), A new parameterization of the absorbance due to the 15 micron band system of carbon dioxide, *J. Geophys. Res.*, *96*, 9013–9019.

Kinnison, D. E., et al. (2006), Sensitivity of chemical tracers to meteorological parameters in the MOZART3 chemical transport model, *J. Geophys. Res.*, submitted.

Kockarts, G. (1980), Nitric oxide cooling in the terrestrial thermosphere, *Geophys. Res. Lett.*, *7*, 137–140.

Krüger, K., B. Naujokat, and K. Labitzke (2005), The unusual midwinter warming in the Southern Hemisphere stratosphere 2002: A comparison to Northern Hemisphere phenomena, *J. Atmos. Sci.*, *62*, 603–613.

Lahoz, W. A. (2000), Northern Hemisphere winter stratospheric variability in the Met Office Unified Model, *Q. J. R. Meteorol. Soc.*, *126*, 2605–2630.

Langematz, U., M. Kunze, K. Krger, K. Labitzke, and G. L. Roff (2003), Thermal and dynamical changes of the stratosphere since 1979 and their link to ozone and $CO_2$ changes, *J. Geophys. Res.*, *108*(D1), 4027, doi:10.1029/2002JD002069.

Lanzante, J., S. Klein, and D. J. Seidel (2003), Temporal homogenization of monthly radiosonde data. Part I: Methodology, *J. Clim.*, *16*, 224–240.

Lin, S.-J. (2004), A "vertically-Lagrangian" finite-volume dynamical core for global atmospheric models, *Mon. Weather Rev.*, *132*, 2293–2307.

Lindzen, R. S. (1981), Turbulence and stress due to gravity wave and tidal breakdown, *J. Geophys. Res.*, *86*, 9701–9714.

Maeda, S., T. J. Fuller-Rowell, and D. S. Evans (1989), Zonally averaged dynamical and compositional response of the thermosphere to auroral activity during September 18–24, 1984, *J. Geophys. Res.*, *94*, 16,869–16,883.

Manzini, E., B. Steil, C. Brühl, M. A. Giorgetta, and K. Krger (2003), A new interactive chemistry-climate model: 2. Sensitivity of the middle atmosphere to ozone depletion and increase in greenhouse gases and implications for recent stratospheric cooling, *J. Geophys. Res.*, *108*(D14), 4429, doi:10.1029/2002JD002977.

Marsh, D. R., S. C. Solomon, and A. E. Reynolds (2004), Empirical model of nitric oxide in the lower thermosphere, *J. Geophys. Res.*, *109*, A07301, doi:10.1029/2003JA010199.

McFarlane, N. A. (1987), The effect of orographically excited gravity wave drag on the general circulation of the lower stratosphere and troposphere, *J. Atmos. Sci.*, *44*, 1775–1800.

McIntyre, M. E. (1989), Dynamics and transport near the polar mesopause in summer, *J. Geophys. Res.*, *94*, 14,617–14,628.

Mlynczak, M. G., and S. Solomon (1993), A detailed evaluation of the heating efficiency in the middle atmosphere, *J. Geophys. Res.*, *98*, 10,517–10,541.

Mote, P. W., K. H. Rosenlof, M. E. McIntyre, E. W. Carr, J. C. Gille, J. R. Holton, J. S. Kinnersley, H. C. Pumphrey, J. M. Russell, and J. W. Waters (1996), An atmospheric tape recorder: The imprint of tropical tropopause temperatures on stratospheric water vapor, *J. Geophys. Res.*, *101*, 3989–4006.

Newchurch, M. J., E. Yang, D. M. Cunnold, G. C. Reinsel, J. M. Zawodny, and J. M. Russell III (2003), Evidence for slowdown in stratospheric ozone loss: First stage of ozone recovery, *J. Geophys. Res.*, *108*(D16), 4507, doi:10.1029/2003JD003471.

Oltmans, S. J., H. Volmel, D. J. Hofmann, K. Rosenlof, and D. Kley (2002), The increase in stratospheric water vapor from balloon borne frostpoint hygrometer measurements at Washington, D. C. and Boulder, Colorado, *Geophys. Res. Lett.*, *27*, 3453–3456.

Pawson, S., and B. Naujokat (1999), The cold winters of the middle 1990s in the northern lower stratosphere, *J. Geophys. Res.*, *104*, 14,209–14,222.

Pickering, K. E., Y. Wang, W. Tao, C. Price, and J. Müller (1998), Vertical distributions of lightning $NO_x$ for use in regional and global chemical transport models, *J. Geophys. Res.*, *103*(D23), 31,203–31,216.

Plumb, R. A. (1996), A "tropical pipe" model of stratospheric transport, *J. Geophys. Res.*, *101*, 3957–3972.

Plumb, R. A., and R. C. Bell (1982), Model of the quasi-biennial oscillation on an equatorial beta-plane, *Q. J. R. Meteorol. Soc.*, *108*, 335–352.

Price, C., J. Penner, and M. Parther (1997a), $NO_x$ from lightning: 1. Global distribution based on lightning physics, *J. Geophys. Res.*, *102*, 5929–5941.

Price, C., J. Penner, and M. Prather (1997b), $NO_x$ from lightning 2. Constraints from the global atmospheric electric circuit, *J. Geophys. Res.*, *102*, 5943–5952.

Randel, W. J., and F. Wu (2006a), Biases in stratospheric and tropospheric temperature trends derived from historical radiosonde data, *J. Clim.*, *19*, 2094–2104.

Randel, W. J., and F. Wu (2006b), A stratospheric ozone profile data set for 1979–2005: Variability, trends, and comparisons with column ozone data, *J. Geophys. Res.*, submitted.

Randel, W. J., R. R. Garcia, and F. Wu (2001), Time-dependent upwelling in the tropical lower stratosphere estimated from the zonal-mean momentum budget, *J. Atmos. Sci.*, *59*, 2141–2152.

Randel, W., et al. (2004a), The SPARC Intercomparison of middle-atmosphere climatologies, *J. Clim.*, *17*, 986–1003.

Randel, W. J., F. Wu, S. J. Oltmans, K. Rosenlof, and G. E. Nedoluha (2004b), Interannual changes of stratospheric water vapor and correlations with tropical tropopause temperatures, *J. Atmos. Sci.*, *61*, 2133–2148.

Richmond, A. D., et al. (1980), An empirical model of quiet-day ionospheric electric fields at middle and low latitudes, *J. Geophys. Res.*, *85*, 4658–4664.

Richter, A., F. Wittrock, M. Weber, S. Beirle, S. Kühl, U. Platt, T. Wagner, W. Wilms-Grabe, and J. P. Burrows (2005), GOME Observations of stratospheric trace gas distributions during the splitting vortex event in the Antarctic winter of 2002. Part I: Measurements, *J. Atmos. Sci.*, *62*, 778–785.

Roble, R. G., and E. C. Ridley (1987), An auroral model for the NCAR thermospheric general circulation model (TGCM), *Ann. Geophys.*, *87*, 369–382.

Roble, R. G., and E. C. Ridley (1994), A thermosphere-ionosphere-mesosphere-electrodynamics general circulation model (TIME-GCM): Equinox solar cycle minimum simulations (30–500 km), *Geophys. Res. Lett.*, *21*, 417–420.

Roble, R. G., R. E. Dickinson, and E. C. Ridley (1982), Global circulation and temperature structure of thermosphere with high-latitude plasma convection, *J. Geophys. Res.*, *87*, 1599–1614.

Roscoe, H. K., J. D. Shanklin, and S. R. Colwell (2005), Has the Antarctic vortex split before 2002?, *J. Atmos. Sci.*, *62*, 581–588.

Salby, M. L. (1982), Sampling theory for asynoptic satellite observations. part II: Fast Fourier synoptic mapping, *J. Atmos. Sci.*, *39*, 2601–2614.

Sander, S. P., et al. (2003), Chemical kinetics and photochemical data for use in atmospheric studies, Evaluation Number 14, *JPL Publ., 02-25*.

Sassi, F., R. R. Garcia, B. A. Boville, and H. Liu (2002), On temperature inversions and the mesospheric surf zone, *J. Geophys. Res.*, *107*(D19), 4380, doi:10.1029/2001JD001525.

Scaife, A. A., N. Butchart, D. R. Jackson, and R. Swinbank (2003), Can changes in ENSO activity help to explain increasing stratospheric water vapor?, *Geophys. Res. Lett.*, *30*(17), 1880, doi:10.1029/2003GL017591.

Schmidt, H., G. P. Brasseur, M. Charron, E. Manzini, M. A. Giorgetta, T. Diehl, V. I. Fomichev, D. Kinnison, D. Marsh, and S. Walters (2006), The HAMMONIA chemistry climate model: Sensitivity of the mesopause region to the 11-year solar cycle and $CO_2$ doubling, *J. Clim.*, *19*, 3903–3931.

Shine, K. P., et al. (2003), A comparison of model-simulated trends in stratospheric temperatures, *Q. J. R. Meteorol. Soc.*, *129*, 1565–1588.

Solomon, S. C., and L. Qian (2005), Solar extreme-ultraviolet irradiance for general circulation models, *J. Geophys. Res.*, *110*, A10306, doi:10.1029/2005JA011160.

Stenchikov, G., A. Robock, V. Ramaswamy, M. D. Schwarzkopf, K. Hamilton, and S. Ramachandran (2002), Arctic Oscillation response to the 1991 Mount Pinatubo eruption: Effects of volcanic aerosols and ozone depletion, *J. Geophys. Res.*, *107*(D24), 4803, doi:10.1029/2002JD002090.

Stolarski, R. S., R. D. McPeters, and P. A. Newman (2005), The ozone hole of 2002 as measured by TOMS, *J. Atmos. Sci.*, *62*, 716–720.

Stolarski, R. S., A. R. Douglass, S. Steenrod, and S. Pawson (2006), Trends in stratospheric ozone: Lessons learned from a 3D chemical transport model, *J. Atmos. Sci.*, *63*, 1028–1041.

Swinbank, R., and D. A. Ortland (2003), Compilation of wind data for the Upper Atmosphere Research Satellite (UARS) Reference Atmosphere Project, *J. Geophys. Res.*, *108*(D19), 4615, doi:10.1029/2002JD003135.

Thomason, L. W., L. R. Poole, and T. Deshler (1997), A global climatology of stratospheric aerosol surface area density measurements: 1984–1994, *J. Geophys. Res.*, *102*, 8967–8976.

Weimer, D. R. (1995), Models of high-latitude electric potentials derived with a least error fit of spherical harmonic coefficients, *J. Geophys. Res.*, *100*, 19,595–19,608.

Woods, T., and G. Rottman (2002), Solar ultraviolet variability over time periods of aeronomic interest, in *Atmospheres in the Solar System: Comparative Aeronomy*, *Geophys. Monogr. Ser.*, vol. 130, edited by M. Mendillo, A. Nagy, and J. H. Waite, pp. 221–234, AGU, Washington, D. C.

World Meteorological Organization (WMO) (2003), *Scientific Assessment of Ozone Depletion: 2002*, *Rep. 47*, 498 pp., Global Res. and Monit. Proj., Geneva.

B. A. Boville, R. R. Garcia, D. E. Kinnison, D. R. Marsh, and F. Sassi, Earth and Sun Systems Laboratory, National Center for Atmospheric Research, P. O. Box 3000, Boulder, CO 80307-3000, USA. (rgarcia@ucar.edu)